Available online at www.sciencedirect.com

ScienceDirect

International Journal of Solids and Structures 44 (2007) 7021–7048

INTERNATIONAL JOURNAL OF SOLIDS AND STRUCTURES

www.elsevier.com/locate/ijsolstr

Confinement-sensitive plasticity constitutive model for concrete in triaxial compression

Vassilis K. Papanikolaou *, Andreas J. Kappos

Laboratory of Reinforced Concrete and Masonry Structures, Civil Engineering Department, Aristotle University of Thessaloniki, P.O. Box 482, Thessaloniki 54124, Greece

Received 12 October 2006; received in revised form 7 March 2007; accepted 24 March 2007
Available online 30 March 2007

Abstract

In this paper, a confinement-sensitive plasticity constitutive model for concrete in triaxial compression is presented, aiming to describe the strength and deformational behaviour of both normal and high-strength concrete under multiaxial compression. It incorporates a three-parameter loading surface, uncoupled hardening and softening functions following the accumulation of plastic volumetric strain and a nonlinear Lode-angle dependent plastic potential function. The various model parameters are calibrated mainly on the basis of a large experimental database and are expressed in terms of only the uniaxial compressive concrete strength, leading to a single-parameter model, suitable for practical applications. The model's performance is evaluated against experimental results and it is found that both the increased strength and deformation capacity of confined concrete are properly captured.

Keywords: Concrete; Confinement; Plasticity; Constitutive modelling; Triaxial compression; Deformation capacity; 3D finite elements

1. Introduction

Three-dimensional finite element analysis of confined concrete members such as columns and bridge piers of arbitrary section (Papanikolaou and Kappos, 2005) requires sophisticated constitutive models, capable of describing the increased strength and deformation capacity of concrete under multiaxial compressive stress states. Different theories and formulations for constitutive modelling of concrete have been suggested in the literature in the past, characterised by a variable degree of complexity, ranging from phenomenological elastic nonlinear (e.g. Darwin and Pecknold, 1977) to complex endochronic plasticity and microplane models (e.g. Bažant and Prat, 1988). The degree of success for each analytical approach depends on the balance between accuracy and practicality, with the latter often hindered by numerous model parameters, often with blurred physical meaning and hence difficult to calibrate against experimental evidence. In the present study, the target is twofold: the formulation of a concrete constitutive model that successfully simulates the basic aspects of

* Corresponding author. Tel.: +30 2310995662; fax: +30 2310995614.
E-mail address: billy@ee.auth.gr (V.K. Papanikolaou).

0020-7683/$ - see front matter
doi:10.1016/j.ijsolstr.2007.03.022

compressive behaviour in the presence of confinement, and an accompanying calibration scheme based on the minimum possible number of material parameters.

The proposed concrete constitutive model follows the classical theory of incremental plasticity (e.g. Chen and Han, 1988). The main components of the model are: a loading surface appropriate for cementitious materials, hardening and softening functions describing the evolution of the loading surface during plastic flow and an appropriate combination between a hardening/softening parameter and a plastic potential function for correctly estimating the deformation capacity of concrete under triaxial compression. The mathematical description of the above components is presented in the subsequent sections, each one followed by a calibration procedure mainly based on experimental results from the literature. The ensuing values for the various model parameters eventually depend only on the mean uniaxial compressive concrete strength (f_c), which renders the constitutive model to a single-parameter one and hence more convenient for practical applications than multi-parameter models.

It should be noted that since the suggested model is applicable in the concrete compression regime only, it should be properly combined with a tensile fracture model for it to be usable in general finite element applications, where tensile stresses can not be excluded. This combination can be realised by treating plastic and fracture strain separately and apply an iterative scheme to preserve stress equivalence (e.g. De Borst, 1986; Červenka et al., 1998). The development of a complete model and its application to finite element analysis of confined reinforced concrete members is currently under investigation by the writers. Furthermore, the localization of deformations under triaxial compression (Van Mier, 1986) is not currently handled by the current constitutive model; this may introduce mesh dependency in certain applications. However, the softening function can be extended in future studies to either account for the fracture energy of concrete in compression or be associated with deformations instead of strains.

2. Fundamental constitutive equations and definition of the principal stress space

According to the classical theory of plasticity, the incremental total strain vector ($\mathrm{d}\boldsymbol{\varepsilon}$) is decomposed into an elastic ($\mathrm{d}\boldsymbol{\varepsilon}^{\mathrm{e}}$) and a plastic ($\mathrm{d}\boldsymbol{\varepsilon}^{\mathrm{p}}$) component:

$$\mathrm{d}\boldsymbol{\varepsilon} = \mathrm{d}\boldsymbol{\varepsilon}^{\mathrm{e}} + \mathrm{d}\boldsymbol{\varepsilon}^{\mathrm{p}} \tag{1}$$

The reversible elastic strain increments are related to the stress increments through a Hook-type elasticity matrix ($\mathbf{D}$), whose elements involve the concrete elastic modulus (E_c) and the Poisson's ratio (v); values for these elastic parameters will be suggested later (see Appendix A for notation used).

$$\mathrm{d}\boldsymbol{\varepsilon}^{\mathrm{e}} = \mathbf{D}^{-1} \cdot \mathrm{d}\boldsymbol{\sigma} \tag{2}$$

The plastic irreversible strains follow a non-associated flow rule (Eq. (3)), which implies that the direction of the incremental plastic strain vector ($\mathrm{d}\boldsymbol{\varepsilon}^{\mathrm{p}}$) is normal to a plastic potential surface ($g = 0$) that differs from the loading surface ($f = 0$). It is generally accepted (e.g. Smith et al., 1989; Sfer et al., 2002) that a non-associated flow rule can describe the experimentally observed deformation capacity of concrete more closely than its associated counterpart.

$$\mathrm{d}\varepsilon_{ij}^{\mathrm{p}} = \mathrm{d}\lambda \frac{\partial g}{\partial \sigma_{ij}} \tag{3}$$

Both failure and plastic potential surfaces are formulated in the Haigh–Westergaard stress space (Fig. 1), which is defined by the cylindrical coordinates of hydrostatic length (ξ), deviatoric length (ρ) and Lode angle (θ). These coordinates are functions of the invariants (I_1, J_2, J_3) of the principal stress tensor components ($\sigma_1 > \sigma_2 > \sigma_3$, compression negative) according to the following equations:

$$\xi = \frac{I_1}{\sqrt{3}} \quad I_1 = \sigma_1 + \sigma_2 + \sigma_3 \tag{4}$$

$$\rho = \sqrt{2J_2} \quad J_2 = \frac{1}{6}\left[(\sigma_1 - \sigma_2)^2 + (\sigma_2 - \sigma_3)^2 + (\sigma_3 - \sigma_1)^2\right] \tag{5}$$

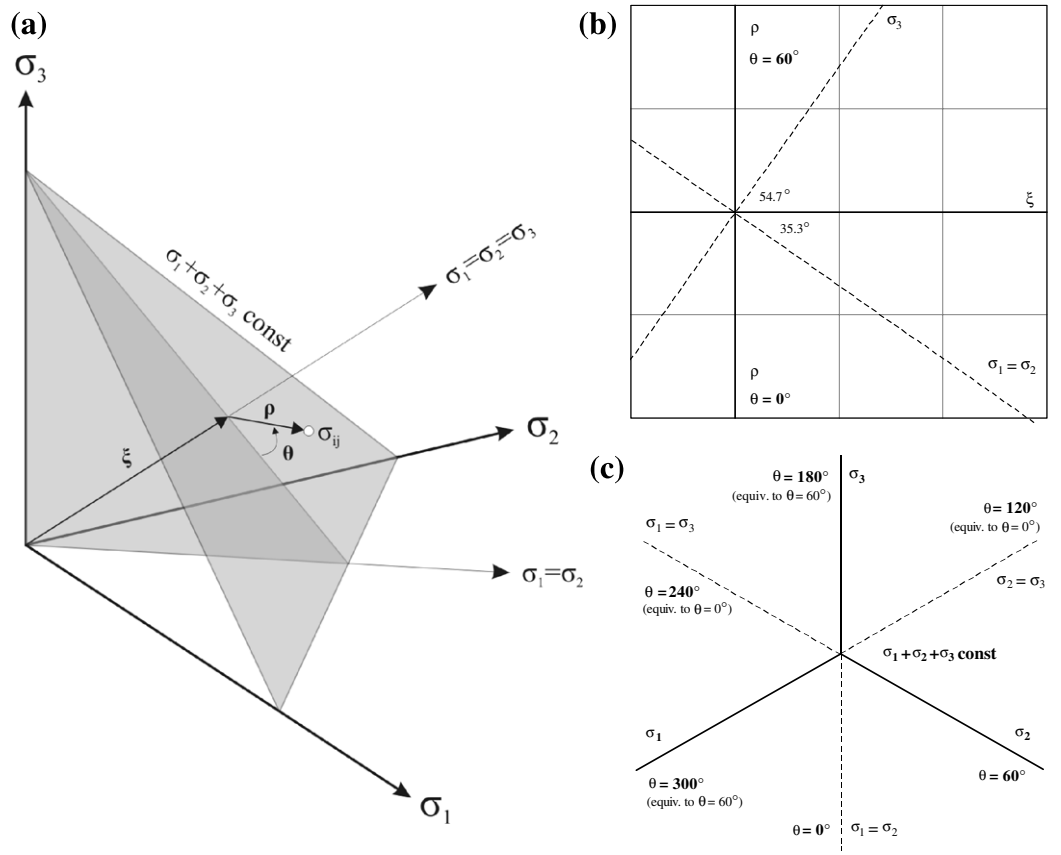

Fig. 1. Coordinates in the Haigh–Westergaard stress space: (a) in the three-dimensional stress space; (b) on the Rendulic plane; (c) on the deviatoric plane.

$$\theta = \frac{1}{3}\cos^{-1}\left(\frac{3\sqrt{3}}{2}\frac{J_3}{J_2^{3/2}}\right) \quad J_3 = (\sigma_1 - I_1/3)\cdot(\sigma_2 - I_1/3)\cdot(\sigma_3 - I_1/3) \tag{6}$$

3. Loading surface

In order to describe the concrete triaxial stress state during plastic flow, a three-parameter hydrostatic-pressure-sensitive loading surface was selected from the literature (Menétrey and Willam, 1995). This surface has parabolic meridians and a variable shape on the deviatoric plane, from triangular to almost circular with increasing confinement. It is described by the following equation, in terms of Haigh–Westergaard coordinates:

$$f(\xi,\rho,\theta) = \left(\sqrt{1.5}\frac{\rho}{k(\kappa)\cdot f_c}\right)^2 + m\left(\frac{\rho}{\sqrt{6}\cdot k(\kappa)\cdot f_c}\mathrm{r}(\theta,e) + \frac{\xi}{\sqrt{3}\cdot k(\kappa)\cdot f_c}\right) - \mathrm{c}(\kappa) = 0 \tag{7}$$

where the friction parameter (m) and the elliptic function (r) are defined as follows:

$$m = 3\frac{(k(\kappa)\cdot f_c)^2 - f_t^2}{k(\kappa)\cdot f_c\cdot f_t}\cdot\frac{e}{e+1} \tag{8}$$

$$r(\theta,e) = \frac{4(1-e^2)\cos^2\theta + (2e-1)^2}{2(1-e^2)\cos\theta + (2e-1)[4(1-e^2)\cos^2\theta + 5e^2 - 4e]^{1/2}} \tag{9}$$

The three parameters that define the shape and size of the loading surface in stress space are the mean uniaxial compressive concrete strength (f_c), the mean uniaxial tensile concrete strength (f_t) and the eccentricity parameter of out-of-roundness (e), discussed later on. Hardening and softening are controlled by functions $k(\kappa)$ and $c(\kappa)$, respectively, and will be described in the subsequent section in detail. In order to calibrate the above three parameters, the loading surface is fixed to its failure (ultimate) state (Fig. 2) by assigning values of unity to functions $k(\kappa)$ and $c(\kappa)$.

Apart from the concrete compressive strength (f_c), which is a free parameter, the other two parameters (f_t and e) can be calibrated against f_c. For calibrating the concrete tensile strength (f_t), two different approaches were followed, namely a code-based equation, applicable to both normal and high-strength concrete (CEB Working Group on HSC/HPC, 1995) and a constant f_c/f_t ratio approach (e.g. Ottosen, 1977; Menétrey and Willam, 1995). In order to evaluate the applicability of each method, an experimental database based on the existing literature was compiled, consisting of triaxial compressive tests of both normal and high-strength cylindrical concrete specimens. Fig. 3 shows a comparison between experimental and analytical values of concrete triaxial strength (f_{cc}). It is observed that while the code equation provides a fairly good correlation between experimental and analytical results (50° trendline), the constant ratio approach with an optimum value of $f_c/f_t = 10$ shows excellent correlation (45° trendline) and hence is suggested for the tensile strength calibration. Fig. 4 shows a comparison between the compressive meridian of the calibrated failure surface ($\theta = 60°$) and experimental results.

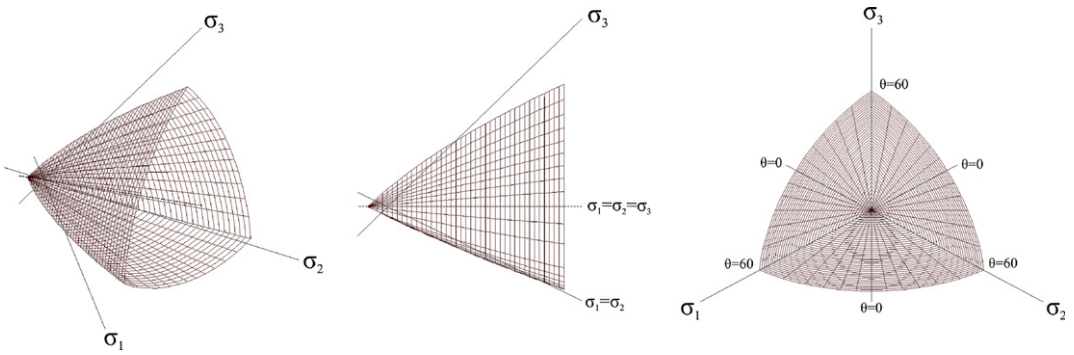

Fig. 2. The three-parameter loading surface in its failure state ($k = c = 1$).

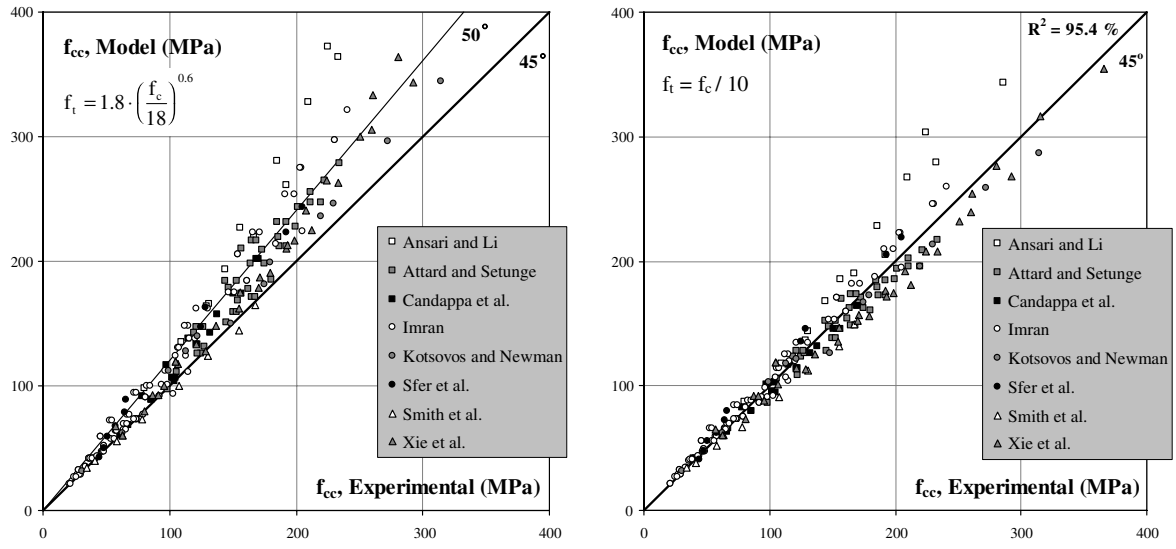

Fig. 3. Calibration of concrete tensile strength (f_t).

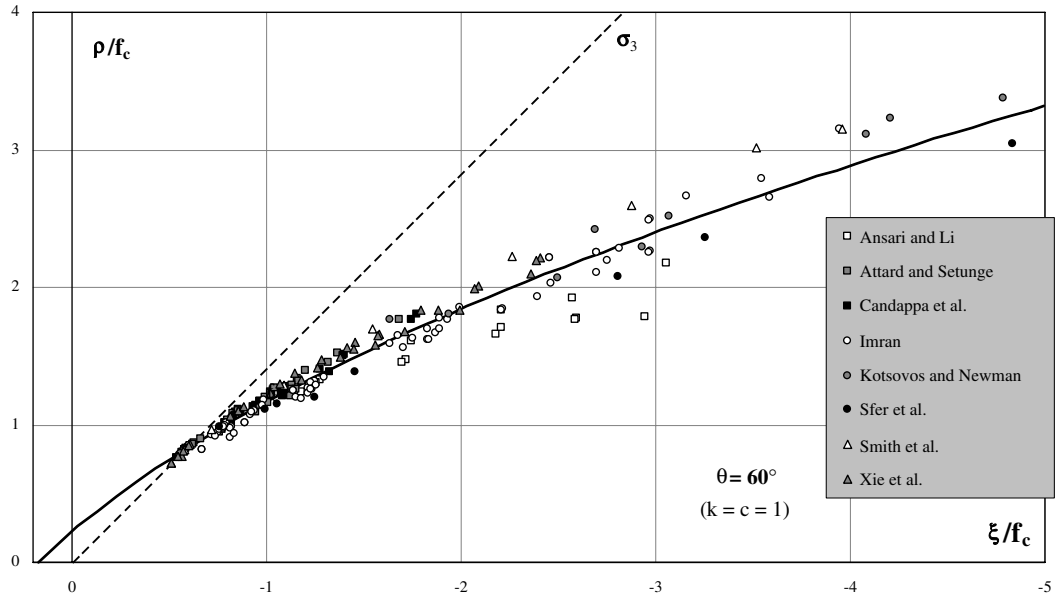

Fig. 4. Comparison between the compressive meridian of the calibrated failure surface ($\theta = 60°$ and $f_c/f_t = 10$) and experimental results on the Rendulic plane.

It should be noted here that the constant f_c/f_t ratio approach may not describe well the true experimental tensile strength of concrete (especially high-strength) as reflected in code equations (e.g. CEB, 1993; CEB Working Group on HSC/HPC, 1995). Nevertheless, it is proposed herein because it provides good agreement with experimental evidence for the adopted failure surface formulation. However, in the context of a compression model for concrete, the accuracy of the tensile strength is not a critical issue, since compression models are usually combined with fracture tensile models that include the true value of tensile strength, in order to handle the tensile concrete behaviour (Červenka et al., 1998).

The eccentricity parameter of out-of-roundness (e) affects the shape of the failure surface in the deviatoric section and can take values from 0.5 (triangular shape) to unity (circular shape). Since this parameter mostly affects the curvature of the tensile meridian ($\theta = 0°$), it is usually calibrated against the equibiaxial compressive concrete strength (f_{bc}). Menétrey and Willam (1995) have suggested a usable range of $0.5 < e \leqslant 0.6$ for concrete, with an optimal value of 0.52, leading to a constant equibiaxial strength $f_{bc} = 1.14 \cdot f_c$ (for $f_c/f_t = 10$). This value has long been assumed adequate for normal concrete, based on the experiments of Kupfer et al. (1969). Nevertheless, recent studies on high-strength concrete (Traina and Mansour, 1991; Hussein and Marzouk, 2000) showed that the ratio between equibiaxial and uniaxial concrete strength decreases with increasing concrete strength, hence a more refined calibration for the eccentricity parameter is necessary. Fig. 5 shows the relationship between the ratio f_{bc}/f_c and uniaxial concrete strength (f_c), based on various experimental studies. A power regression yields the following equation:

$$f_{bc}/f_c = 1.5 \cdot f_c^{-0.075} \tag{10}$$

Although the scatter of the results is substantial (due to different specimen sizes, end conditions and loading setups used by different researchers), this equation describes well the observed trend of reducing f_{bc}/f_c ratio for increasing concrete strength, as opposed to adopting a constant value of 1.14. Table 1 shows the iteratively calculated values for the eccentricity parameter (e) that leads to the equibiaxial strength (f_{bc}) suggested by the above equation. It is clear that the sensitivity to the eccentricity parameter (e) is large, since a variation of about 0.02 amplifies the equibiaxial concrete strength by 15% of f_c.

In Fig. 6 data from the experimental database compiled on the basis of 306 tests (this is a substantially expanded version of the database used in the previous study by Menétrey and Willam (1995)) for the validation of the loading surface, including non-cylindrical specimens and triaxial load paths with $\theta = 0°$, is plotted

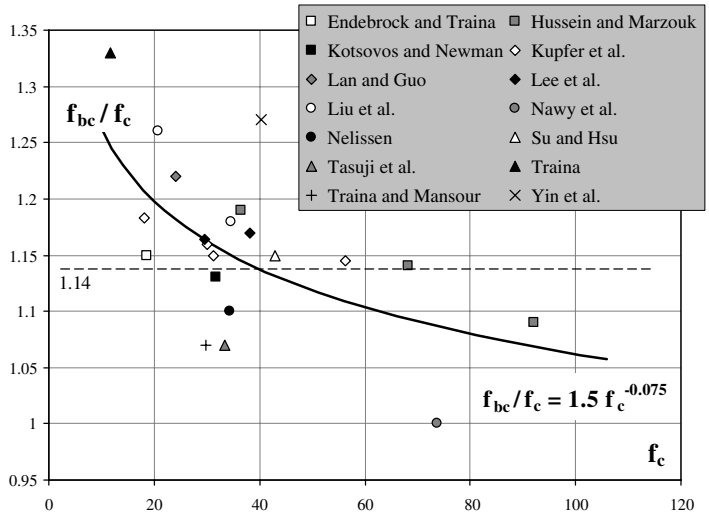

Fig. 5. Relationship between f_{bc}/f_c and uniaxial concrete strength.

Table 1
Suggested values for the eccentricity parameter (e) for various concrete strengths

f_c (MPa)	f_{bc}/f_c	e
20	1.20	0.5281
30	1.16	0.5232
40	1.14	0.5198
50	1.12	0.5172
60	1.10	0.5151
70	1.09	0.5133
80	1.08	0.5117
90	1.07	0.5104
100	1.06	0.5092
110	1.05	0.5081
120	1.05	0.5071

against the three-parameter failure surface. Reasonable correlation is generally observed, especially for low and moderate levels of confinement ($\xi/f_c > -2$), which are the ones more pertinent to practical situations. Therefore, the selected failure surface is considered adequate for describing the confined concrete strength under various load paths.

4. Hardening and softening parameter and functions

Hardening and softening of concrete can be simulated by varying the shape and location of the loading surface during plastic flow. This variation is controlled by a hardening/softening parameter (κ) which is usually defined as the length of the plastic strain vector or by the equivalence of plastic work (e.g. Han and Chen, 1985). However, this approach fails to describe the increased deformation capacity of concrete under multiaxial compression (e.g. Ohtani and Chen, 1989) and therefore, various scaling techniques (referred as ductility or confinement functions), depending on the current stress level (e.g. Barros, 2001) or the plastic volumetric strain (Imran and Pantazopoulou, 2001) have been suggested, with varying degrees of success. The disadvantage of these techniques is that they increase the required number of material parameters (some of them with weak or no physical meaning) and hence complicate the calibration procedure. In order to overcome the above difficulties, the hardening/softening parameter in the present model is set equal to the plastic volumetric strain (ε_v^p), as originally suggested by Grassl et al. (2002). When combined with a properly calibrated nonlinear

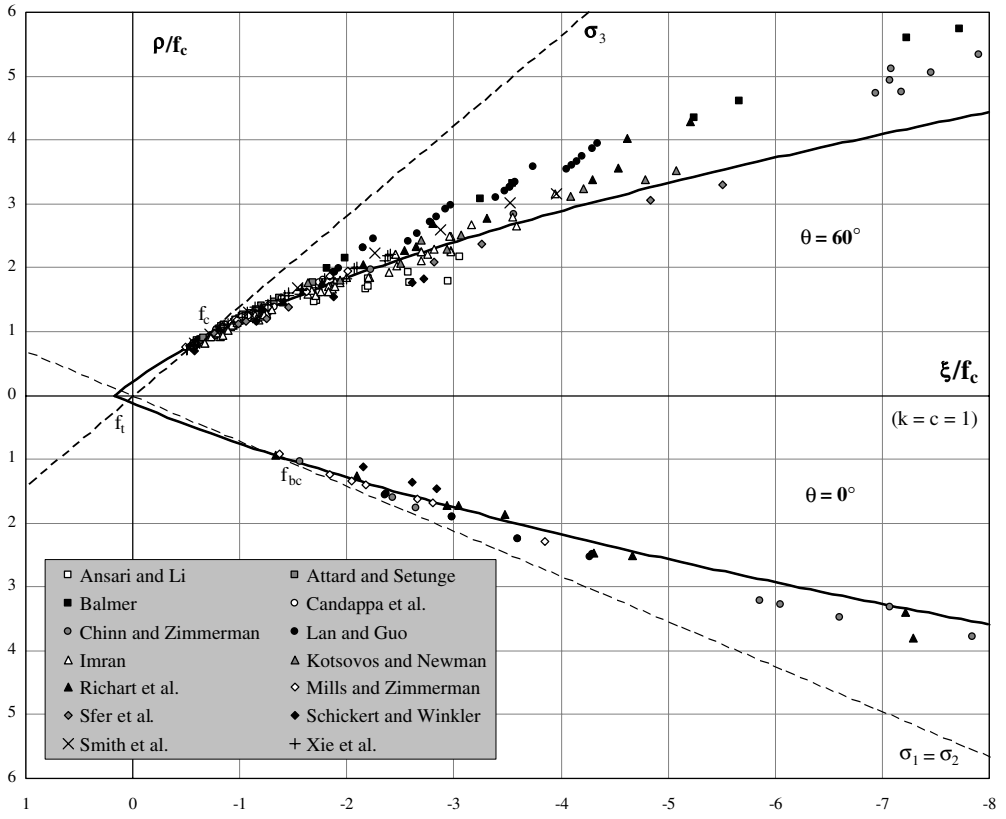

Fig. 6. Comparison between the three-parameter failure surface and experimental results on the Rendulic plane.

plastic potential function (g), it can successfully describe the confined deformation capacity of concrete without any scaling modifications.

$$d\kappa = d\varepsilon_v^p \tag{11}$$

The instantaneous shape and location of the loading surface during hardening is defined by a hardening function (k), which depends on the hardening/softening parameter (κ) i.e. the plastic volumetric strain ($\kappa = \varepsilon_v^p$). This function is directly incorporated in the loading surface equations (7) and (8), operating as a scaling factor for the compressive concrete. It has the following elliptic form (Červenka et al., 1998):

$$k(\kappa) = k(\varepsilon_v^p) = k_o + (1 - k_o) \cdot \sqrt{1 - \left(\frac{\varepsilon_{v,t}^p - \varepsilon_v^p}{\varepsilon_{v,t}^p}\right)^2} \tag{12}$$

where $\varepsilon_{v,t}^p$ is the plastic volumetric strain at uniaxial concrete strength and will be discussed in detail later.

During the hardening process, the softening function (c) in Eq. (7) holds a constant value of unity. Before any plastic deformation occurs ($\varepsilon_v^p = 0$), the hardening function holds a constant value of k_o, defining the initial yield surface that bounds the initial elastic regime.

$$k_o = \sigma_{co}/f_c \tag{13}$$

where σ_{co} is the uniaxial concrete stress defining the onset of plastic flow ($\sigma_{co} > f_t$ for the loading surface equations to be valid). It is experimentally observed that normal concrete behaves almost elastically up to about 30–40% of its uniaxial strength and hence a value of $k_o = 0.3$–0.4 would be adequate. However, in order to account for high-strength concrete, which features a higher initial elastic regime, a more refined calibration was performed, based on the code provisions of MC90 (CEB, 1993) and the recommendations of the CEB

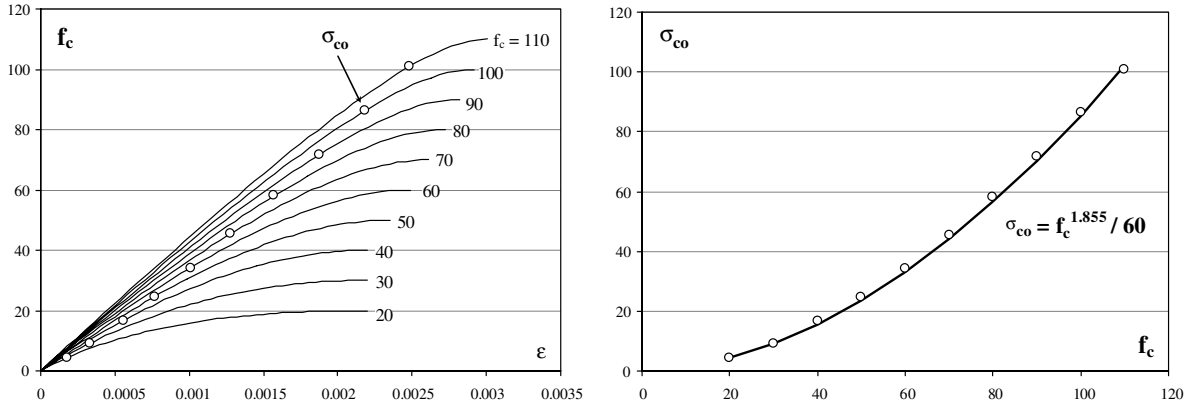

Fig. 7. Calibration of the concrete stress defining the onset of plastic flow (σ_{co}) using MC90 (CEB, 1993) and CEB WG on HSC/HPC (1995) equations.

Working Group on HSC/HPC (1995). Fig. 7(left) shows the uniaxial stress–strain curves of concrete suggested by the aforementioned documents.

It is herein assumed that the initial elastic regime holds until the secant concrete modulus drops to 90% of the initial tangent modulus. The value of σ_{co} is then equal to the respective concrete uniaxial stress value (Fig. 7, right). Following a power regression, the suggested relationship between σ_{co} and f_c is:

$$\sigma_{co} = f_c^{1.855}/60 \tag{14}$$

Based on the previous assumption, the concrete elastic modulus incorporated in the elasticity matrix (Eq. (2)) is set equal to 90% of the initial tangent modulus suggested by the CEB Working Group on HSC/HPC (1995) and is applicable to all concrete grades:

$$E_c = 0.90 \cdot 22000 \cdot \left(\frac{f_c}{10}\right)^{0.3} \tag{15}$$

Moreover, the Poisson's ratio of concrete is assumed to take a constant value of 0.2 (CEB, 1993; Rashid et al., 2002); such a constant value is deemed appropriate in the context of a plasticity formulation.

After the initiation of plastic flow, the accumulation of the plastic volumetric strain continues until a threshold value ($\varepsilon^p_{v,t}$) is reached. This value defines the termination of the hardening process, resulting to value of unity for the hardening function (Eq. (12)). At this stage, the loading surface reaches its failure state and the softening process is initiated. In order to calibrate the threshold value of plastic volumetric strain, it is assumed that the total volumetric strain (ε_v) at peak stress (f_c) under uniaxial compression is equal to zero (Van Mier, 1986; Imran and Pantazopoulou, 1996; Grassl et al., 2002), resulting to a plastic volumetric strain equal to its elastic counterpart (Eq. 16). This threshold value for the plastic volumetric strain is assumed invariable for all other stress states.

$$\varepsilon^p_{v,t} = \frac{f_c}{E_c}(1-2\nu) \tag{16}$$

Fig. 8 shows the evolution of the loading surface during hardening in various geometric representations.

Upon further plastic flow, the hardening function retains a constant value of unity and the material enters the softening regime, which is controlled by the softening function (c). This function simulates the material decohesion by shifting the loading surface along the negative hydrostatic axis. It is assumed that it follows the softening function originally proposed by Van Gysel and Taerwe (1996) for uniaxial compression (Eq. 17), also adopted by the CEB Working Group on HSC/HPC (1995), although it is described herein in terms of the plastic volumetric strain (ε^p_v). This form of the softening function is deemed to better reflect the experimentally observed softening behaviour of concrete, compared to linear or stepwise linear approaches (e.g.

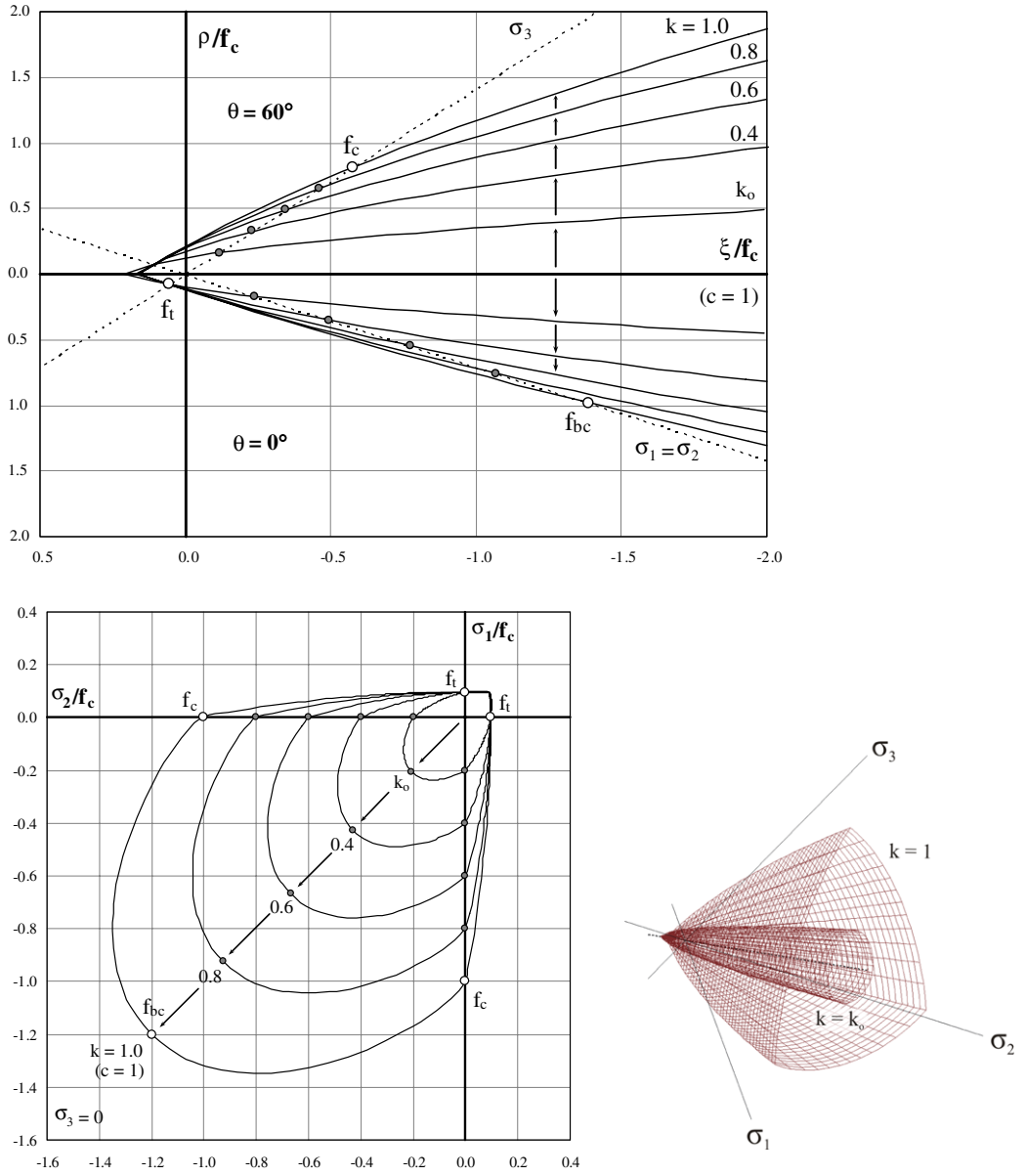

Fig. 8. Evolution of the loading surface during hardening on the Rendulic plane, biaxial plane ($\sigma_3 = 0$) and three-dimensional stress space.

Červenka et al., 1998; Grassl et al., 2002), which also introduce discontinuities in the softening function that may cause numerical instabilities.

$$c(\kappa) = c(\varepsilon_v^p) = \left(\frac{1}{1 + \left(\frac{n_1 - 1}{n_2 - 1}\right)^2} \right)^2 \tag{17}$$

$$n_1 = \varepsilon_v^p / \varepsilon_{v,t}^p \tag{18}$$

$$n_2 = (\varepsilon_{v,t}^p + t)/\varepsilon_{v,t}^p \tag{19}$$

The outmost square in Eq. (17) is necessary due to the quadratic nature of the loading surface. The softening function values start from unity and complete material decohesion is attained at $c = 0$. The

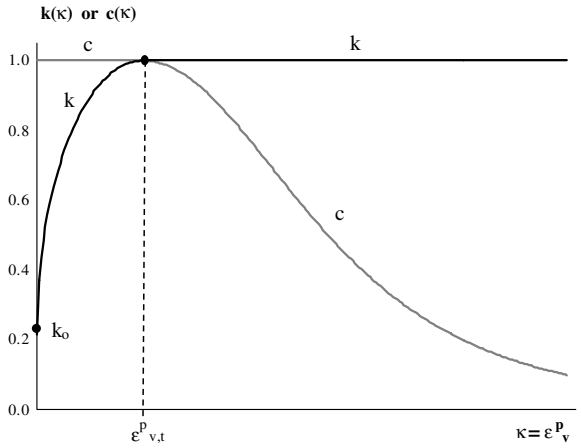

Fig. 9. Evolution of hardening (k) and softening (c) functions with respect to the plastic volumetric strain.

evolution of both hardening and softening functions with respect to the hardening/softening parameter is schematically shown in Fig. 9. The evolution of the loading surface during softening is shown in Fig. 10.

Parameter t in Eq. (19) controls the slope of the softening function and was calibrated against f_c using the following procedure: It was assumed that the present model should produce such a uniaxial stress–strain curve for concrete, that the softening (descending) branch would pass from a predefined control point at $(0.5f_c, \varepsilon_{0.5f_c})$. In order to define the uniaxial compressive strain $(\varepsilon_{0.5f_c})$ that corresponds to $0.5f_c$ for various concrete grades, an experimental database of uniaxial compression tests was compiled (Fig. 11, left). For each test point, the value of the slope parameter (t) that, when introduced in the model, would lead to the respective experimental uniaxial strain $\varepsilon_{0.5f_c}$ was calculated by a trial-and-error procedure (Fig. 11, right) and a linear regression yielded the following simple equation for t:

$$t(‰) = f_c/15 \tag{20}$$

Fig. 12 shows a set of uniaxial stress–strain curves of various concrete grades, as derived by the present model. It is observed that high-strength concrete features, such as the broader initial elastic region and the steeper softening branch (CEB Working Group on HSC/HPC, 1995) are successfully captured. It is noted again that the experimentally observed non-local behaviour of concrete under compression (Van Mier, 1986) is *not* handled by the above formulation. A future enhancement of the softening function could be to either incorporate the crushing fracture energy of concrete or to express the function in terms of deformations instead of strains. However, this would further complicate the calibration procedure since the non-local behaviour is related to structural rather than material properties.

5. Plastic potential function

In the context of a non-associated flow rule, the definition of an appropriate plastic potential function (g) plays a critical role in the correct estimation of the deformation capacity of concrete under triaxial compression. The plastic potential function controls the direction of the plastic strain vector (normal to the plastic potential surface $g = 0$) and hence the relative ratios between the plastic strain tensor components. As a result, it governs the accumulation of the plastic volumetric strain, herein adopted as a hardening/softening parameter (κ), and eventually the evolution of hardening and softening under various load paths. Since the volumetric growth (dilatancy) of concrete depends on the confinement level (e.g. Smith et al., 1989) i.e. it decreases under increasing lateral stresses, the gradient of the plastic potential function should vary along the hydrostatic axis. This can be achieved by either incorporating a linear plastic potential function of Drucker–Prager type with a variable slope (Han and Chen, 1985; Imran and Pantazopoulou, 2001) or a nonlinear function (Grassl et al., 2002). In this study, a polynomial function with the characteristics of Lode-angle (θ) dependency

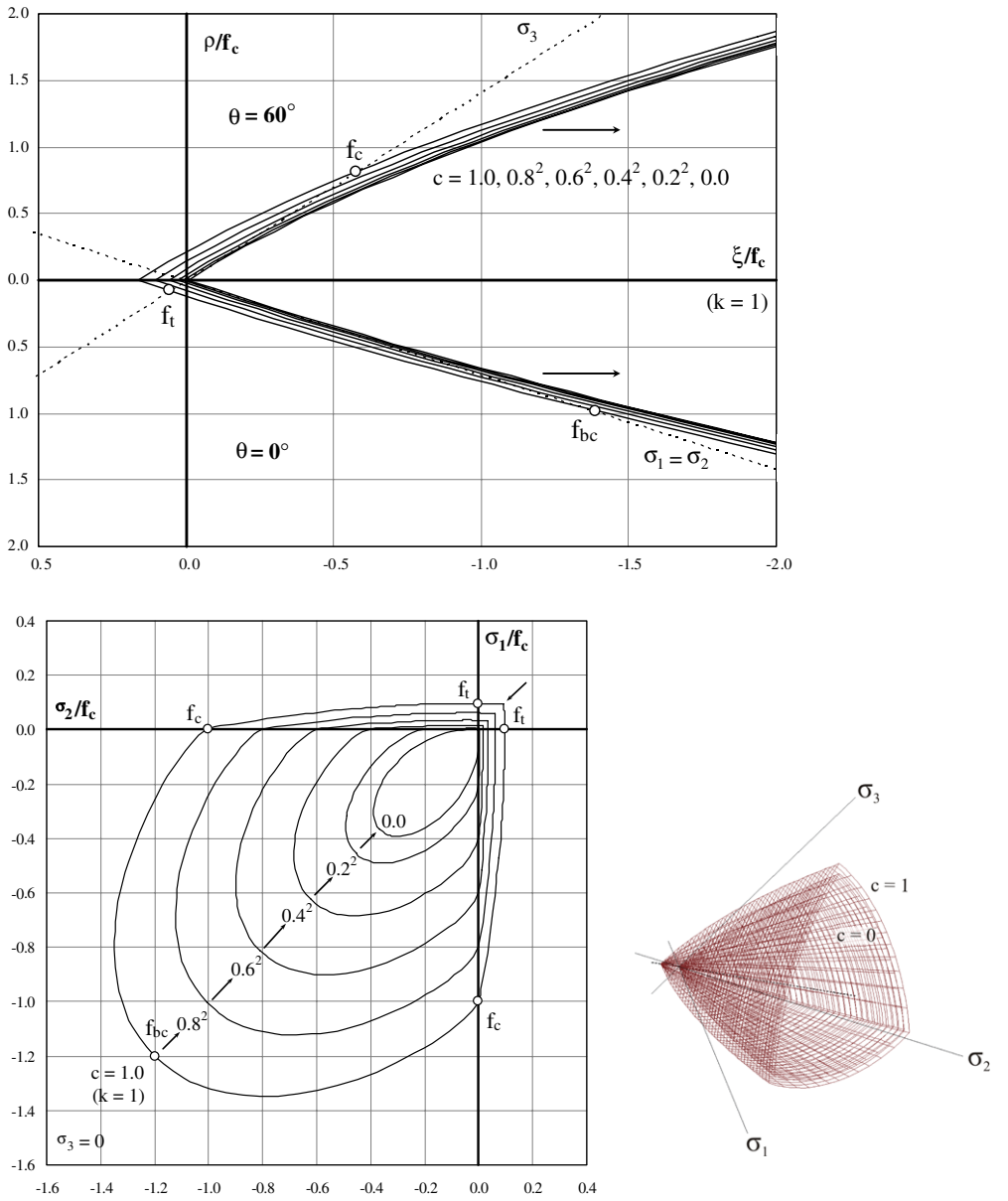

Fig. 10. Evolution of the loading surface during softening on the Rendulic plane, biaxial plane ($\sigma_3 = 0$) and three-dimensional stress space.

and adjustable order (n) is suggested (Eq. (21)); it is noted that these characteristics are not included in other similar constitutive models proposed in the literature (e.g. Imran and Pantazopoulou, 1996; Grassl et al., 2002; Grassl and Jirasek, 2006). The partial derivatives of the plastic potential function with respect to the principal stresses are given in Appendix B.

$$g = A \cdot \left(\frac{\rho}{k \cdot \sqrt{c} \cdot f_c}\right)^n + \left[C + \tfrac{1}{2}(B - C)(1 - \cos 3\theta)\right] \cdot \frac{\rho}{k \cdot \sqrt{c} \cdot f_c} + \frac{\xi}{k \cdot \sqrt{c} \cdot f_c} - a \tag{21}$$

In order to easily calibrate the three plastic potential coefficients A, B and C in Eq. (21), it is assumed that the inclination (ψ) of the incremental plastic strain vector is identical to that of the total plastic strain vector at three distinct stress states, which will be defined later. This inclination is expressed by the angle formed

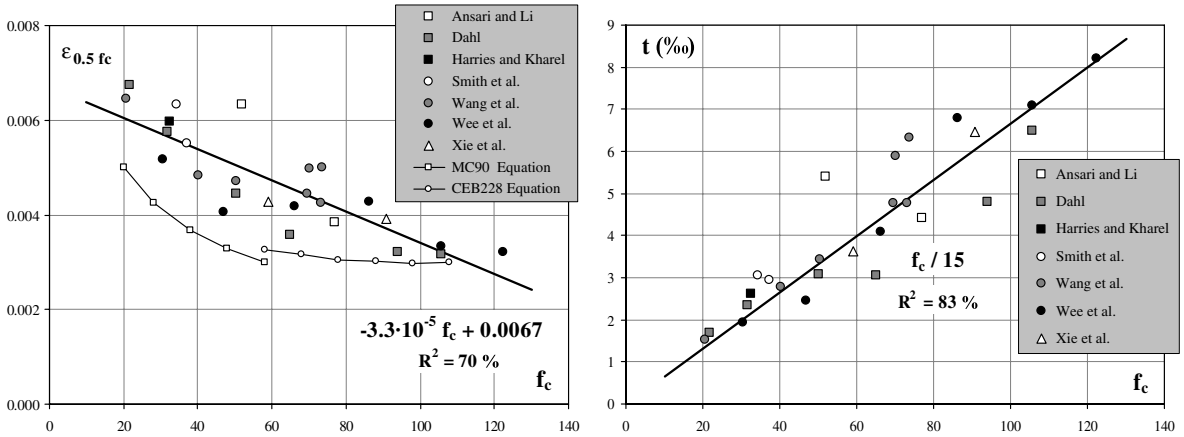

Fig. 11. (Left) Relationship between f_c and experimental uniaxial strain $\varepsilon_{0.5f_c}$ at $0.5f_c$. Results from code equations (CEB, 1993; CEB WG on HSC/HPC, 1995) are included for comparison purposes. (Right) Suggested relationship between f_c and slope parameter t (‰).

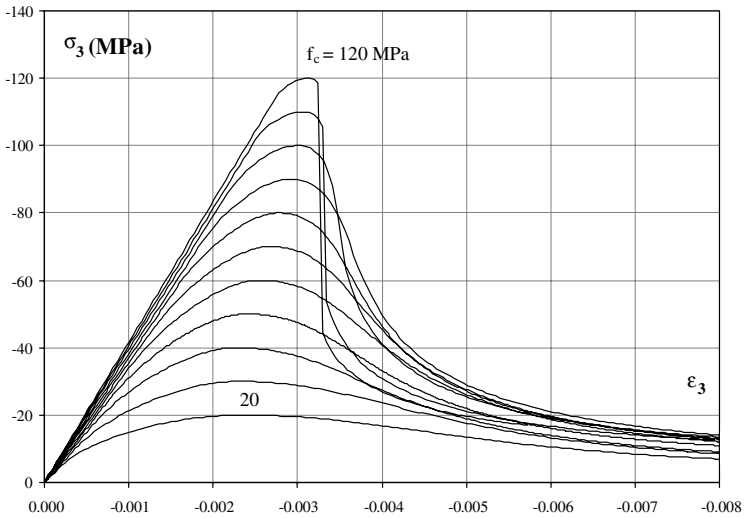

Fig. 12. Uniaxial stress–strain curves for various concrete grades derived by the constitutive model.

between the plastic strain vector and the hydrostatic axis or, equivalently, between the tangent of the plastic potential surface and the deviatoric axis, since the plastic strain vector is always normal to the plastic potential surface (Fig. 13):

$$\psi = \frac{\rho'}{\xi'} = -\frac{\mathrm{d}\xi}{\mathrm{d}\rho} \tag{22}$$

where ξ' and ρ' are the hydrostatic and deviatoric lengths of the total plastic strain vector, respectively (similar to Eqs. (4) and (5), but expressed here in terms of plastic strain).

The necessary stress states (control points) for the definition of coefficients A, B and C in Eq. (21) correspond to the compressive concrete strength under uniaxial, triaxial and equibiaxial compression. Specifically, coefficients A and B are calibrated by the uniaxial and triaxial strength on the compressive meridian ($\theta = 60°$) and C by the equibiaxial strength on the tensile meridian ($\theta = 0°$). The plastic potential function (Eq. 21) is hence set to its failure state, by assigning values of unity to hardening (k) and softening (c) functions:

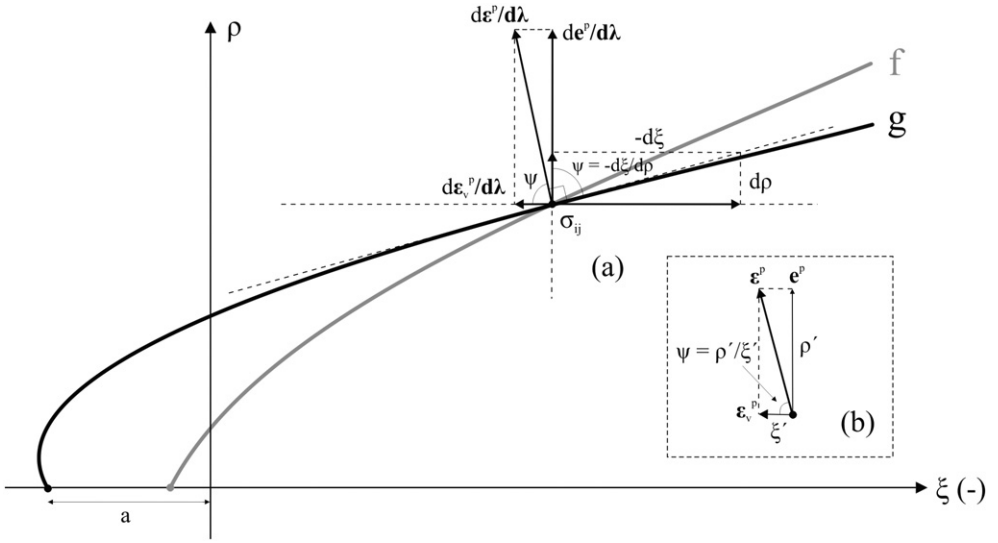

Fig. 13. Direction (ψ) of the incremental (a) and total (b) plastic strain vectors.

$$g = A \cdot \left(\frac{\rho}{f_c}\right)^n + \left[C + \tfrac{1}{2}(B - C)(1 - \cos 3\theta)\right] \cdot \frac{\rho}{f_c} + \frac{\xi}{f_c} - a \tag{23}$$

For the calibration of coefficients A and B on the compressive meridian ($\theta = 60°$), the plastic potential function (Eq. (23)) further reduces to:

$$g = A \cdot \left(\frac{\rho}{f_c}\right)^n + B \cdot \frac{\rho}{f_c} + \frac{\xi}{f_c} - a \tag{24}$$

The inclination ψ is the gradient of the plastic potential surface ($g = 0$) with respect to the deviatoric axis:

$$\psi = -\frac{\mathrm{d}\xi}{\mathrm{d}\rho} = n \cdot A \cdot \left(\frac{\rho}{f_c}\right)^{n-1} + B \tag{25}$$

If ψ_1, ψ_2 are the inclinations of the plastic strain vector and ρ_1, ρ_2 are the deviatoric lengths of the stress vector under uniaxial and triaxial compression, respectively, it follows that:

$$\psi_1 = n \cdot A \cdot \left(\frac{\rho_1}{f_c}\right)^{n-1} + B \tag{26}$$

$$\psi_2 = n \cdot A \cdot \left(\frac{\rho_2}{f_c}\right)^{n-1} + B \tag{27}$$

By solving the system of Eqs. (26) and (27), the following values for coefficients A and B are derived:

$$A = \frac{\psi_1 - \psi_2}{n \cdot \left(\left(\frac{\rho_1}{f_c}\right)^{n-1} - \left(\frac{\rho_2}{f_c}\right)^{n-1}\right)} \tag{28}$$

$$B = \psi_1 - n \cdot A \cdot \left(\frac{\rho_1}{f_c}\right)^{n-1} \tag{29}$$

The coefficient C is calibrated on the tensile meridian $\theta = 0°$ and hence the plastic potential function (Eq. (23)) reduces to:

$$g = A \cdot \left(\frac{\rho}{f_c}\right)^n + C \cdot \frac{\rho}{f_c} + \frac{\xi}{f_c} - a \tag{30}$$

If ψ_3 and ρ_3 are the inclination of the plastic strain vector and the deviatoric length of the stress vector at equibiaxial compression, respectively, it follows that:

$$\psi_3 = -\frac{\mathrm{d}\xi}{\mathrm{d}\rho} = n \cdot A \cdot \left(\frac{\rho_3}{f_c}\right)^{n-1} + C \tag{31a}$$

which leads to

$$C = \psi_3 - n \cdot A \cdot \left(\frac{\rho_3}{f_c}\right)^{n-1} \tag{31b}$$

At this stage, values for ρ_1, ρ_2, ρ_3 and ψ_1, ψ_2, ψ_3 are required in Eqs. (28), (29) and (31b) in order to calculate the plastic potential coefficients A, B and C. The deviatoric lengths ρ_1, ρ_2, ρ_3 depend on the corresponding stress tensors and can be derived as follows:

Uniaxial compression: The calculation of ρ_1 is trivial, depending only on the uniaxial compressive strength (f_c).

$$\rho_1 = \sqrt{2J_2} = \sqrt{2 \cdot \tfrac{1}{6} \cdot \left[(0-0)^2 + (0-f_c)^2 + (f_c-0)^2\right]} = \sqrt{\tfrac{2}{3}} \cdot |f_c| \tag{32}$$

Triaxial compression: The calculation of ρ_2 needs an arbitrarily defined lateral stress (σ_{pc}) and the corresponding triaxial strength (f_{cc}) derived from the current failure surface, using an iterative procedure. Herein, this lateral stress was chosen equal to the uniaxial compressive strength ($\sigma_{pc} = f_c$) and indicative values of f_{cc}, emanating from this iterative procedure, for various concrete grades are shown in Table 2.

$$\rho_2 = \sqrt{2J_2} = \sqrt{2 \cdot \tfrac{1}{6} \cdot \left[(\sigma_{pc}-\sigma_{pc})^2 + (\sigma_{pc}-f_{cc})^2 + (f_{cc}-\sigma_{pc})^2\right]} = \sqrt{\tfrac{2}{3}} \cdot |f_{cc}-\sigma_{pc}| \tag{33}$$

Equibiaxial compression: The calculation of ρ_3 depends on the equibiaxial concrete strength (f_{bc}), already calibrated against f_c, using Eq. (10), hence

$$\rho_3 = \sqrt{2J_2} = \sqrt{2 \cdot \tfrac{1}{6} \cdot \left[(0-f_{bc})^2 + (f_{bc}-f_{bc})^2 + (f_{bc}-0)^2\right]} = \sqrt{\tfrac{2}{3}} \cdot |f_{bc}| \tag{34}$$

The inclinations ψ_1, ψ_2, ψ_3 for uniaxial, triaxial and equibiaxial compression, respectively, depend on the corresponding plastic strain tensors and can be derived using the hydrostatic (ξ') and deviatoric length (ρ') of the plastic strain vector (compressive stresses assume negative values in Eqs. (36), (39) and (42)).

$$\psi = \frac{\rho'}{\xi'} = \frac{\sqrt{2 \cdot \tfrac{1}{6} \cdot \left[(\varepsilon_1^p - \varepsilon_2^p)^2 + (\varepsilon_2^p - \varepsilon_3^p)^2 + (\varepsilon_3^p - \varepsilon_1^p)^2\right]}}{\frac{\varepsilon_1^p + \varepsilon_2^p + \varepsilon_3^p}{\sqrt{3}}} \tag{35}$$

The components of the principal plastic strain tensor under uniaxial compression are:

Table 2
Derived values for the triaxial concrete stress (f_{cc}) from the current failure surface

f_c (MPa)	σ_{pc}	f_{cc}
20	20	87.1
30	30	130.4
40	40	173.6
50	50	216.8
60	60	259.9
70	70	302.9
80	80	346.0
90	90	389.0
100	100	432.0
110	110	474.9
120	120	517.9

$$\varepsilon_3^{\mathrm{p}} = \varepsilon_3 - \varepsilon_3^{\mathrm{e}} = \varepsilon_{\mathrm{c}} - \tfrac{1}{E_{\mathrm{c}}}[f_{\mathrm{c}} - \nu \cdot (0+0)] = \varepsilon_{\mathrm{c}} - \frac{f_{\mathrm{c}}}{E_{\mathrm{c}}} \tag{36}$$

$$\varepsilon_1^{\mathrm{p}} = \varepsilon_2^{\mathrm{p}} = \frac{\varepsilon_{\mathrm{v,p}}^{\mathrm{p}} - \varepsilon_3^{\mathrm{p}}}{2} \tag{37}$$

where $\varepsilon_{\mathrm{v,p}}^{\mathrm{p}} = \frac{f_{\mathrm{c}}}{E_{\mathrm{c}}}(1-2\nu)$ (Eq. (16))

The total strain at uniaxial concrete strength (ε_{c}, Eq. (36)) follows the recommendations of MC90 (CEB, 1993) and CEB Working Group on HSC/HPC (1995) for normal and high-strength concrete, respectively:

$$\varepsilon_{\mathrm{c}} = \min \begin{cases} -0.0022 \\ -\dfrac{0.7 \cdot f_{\mathrm{c}}^{0.31}}{1000} \end{cases} \tag{38}$$

It should be noted here that experimental evidence regarding the dependence of ε_{c} on concrete strength shows considerable scatter, which may be attributed to different concrete mixtures, specimen sizes, end conditions and measurement setups among different researchers (Carreira and Chu, 1985), as well as the relative flatness of the σ–ε curve in the region close to the peak stress. Nevertheless, the above code equation (Eq. (38)) approximates well the experimental results from various researchers (Fig. 14).

The components of the principal plastic strain tensor under triaxial compression are:

$$\varepsilon_3^{\mathrm{p}} = \varepsilon_3 - \varepsilon_3^{\mathrm{e}} = \varepsilon_{\mathrm{cc}} - \tfrac{1}{E_{\mathrm{c}}}[f_{\mathrm{cc}} - \nu \cdot (\sigma_{\mathrm{pc}} + \sigma_{\mathrm{pc}})] = \varepsilon_{\mathrm{cc}} - \tfrac{1}{E_{\mathrm{c}}}[f_{\mathrm{cc}} - 2 \cdot \nu \cdot \sigma_{\mathrm{pc}}] \tag{39}$$

$$\varepsilon_1^{\mathrm{p}} = \varepsilon_2^{\mathrm{p}} = \frac{\varepsilon_{\mathrm{v,p}}^{\mathrm{p}} - \varepsilon_3^{\mathrm{p}}}{2} \tag{40}$$

where $\varepsilon_{\mathrm{v,p}}^{\mathrm{p}} = \frac{f_{\mathrm{c}}}{E_{\mathrm{c}}}(1-2\nu)$, same as in the uniaxial case (Eq. (16))

For the derivation of the total strain at triaxial stress ($\varepsilon_{\mathrm{cc}}$, Eq. (39)), a linear relationship between the confinement level ($\sigma_{\mathrm{pc}}/f_{\mathrm{c}}$) and strain amplification ($\varepsilon_{\mathrm{cc}}/\varepsilon_{\mathrm{c}}$) under triaxial compression is suggested, based on an experimental database (Fig. 15). It is observed that the scatter of the results is wider for higher confinement levels.

$$\varepsilon_{\mathrm{cc}} = \varepsilon_{\mathrm{c}} \cdot \left(1 + 17 \cdot \frac{\sigma_{\mathrm{pc}}}{f_{\mathrm{c}}}\right) \tag{41}$$

which reduces to $\varepsilon_{\mathrm{cc}} = 18 \cdot \varepsilon_{\mathrm{c}}$ for $\sigma_{\mathrm{pc}} = f_{\mathrm{c}}$

The components of the principal plastic strain tensor under equibiaxial compression are:

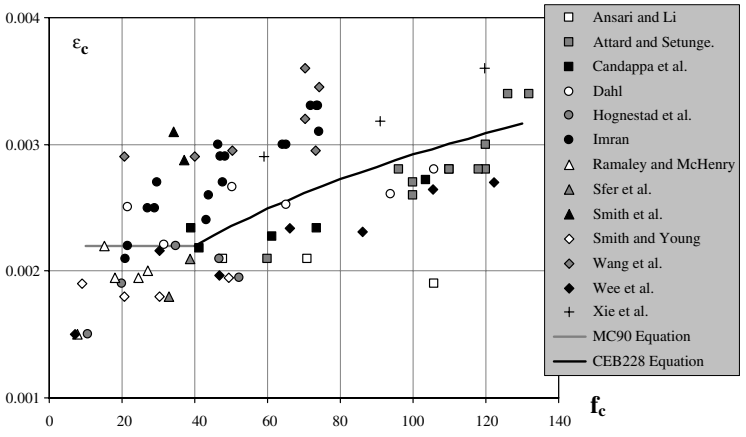

Fig. 14. Relationship between total strain at uniaxial concrete strength (ε_{c}) and concrete strength (f_{c}).

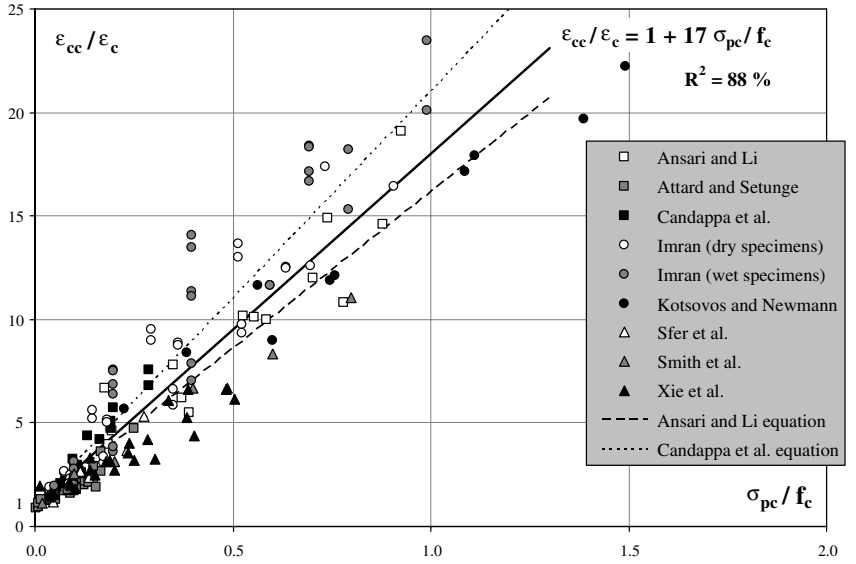

Fig. 15. Relationship between confinement level and strain amplification under triaxial compression.

$$\varepsilon_3^{\mathrm{p}} = \varepsilon_2^{\mathrm{p}} = \varepsilon_3 - \varepsilon_3^{\mathrm{e}} = \varepsilon_{\mathrm{bc}} - \tfrac{1}{E_{\mathrm{c}}}[f_{\mathrm{bc}} - v \cdot (f_{\mathrm{bc}} + 0)] = \varepsilon_{\mathrm{bc}} - \frac{f_{\mathrm{bc}}}{E_{\mathrm{c}}}(1 - v) \tag{42}$$

$$\varepsilon_1^{\mathrm{p}} = \varepsilon_{\mathrm{v,p}}^{\mathrm{p}} - 2 \cdot \varepsilon_3^{\mathrm{p}} \tag{43}$$

where $\varepsilon_{\mathrm{v,p}}^{\mathrm{p}} = \frac{f_{\mathrm{c}}}{E_{\mathrm{c}}}(1 - 2v)$, same as in the uniaxial case (Eq. (16)).

For the calculation of the total strain $\varepsilon_{\mathrm{bc}}$ under equibiaxial compression, the well known expression $\varepsilon_{\mathrm{bc}} = \varepsilon_{\mathrm{c}} \cdot (3 \cdot f_{\mathrm{bc}}/f_{\mathrm{c}} - 2)$ suggested by Darwin and Pecknold (1977), also adopted by MC90 (CEB, 1993) could be used. Nevertheless, this expression seems to overestimate the equibiaxial strains compared to the majority of experimental evidence, which show marginal to zero strain amplifications under equibiaxial loading (Liu et al., 1972; Yin et al., 1989; Traina and Mansour, 1991; Hussein and Marzouk, 2000; Lee et al., 2004). Unless a more comprehensive database becomes available, a reasonable alternative is to assume that strains and stresses are equally amplified under equibiaxial compression (Eq. (10)):

$$\varepsilon_{\mathrm{bc}}/\varepsilon_{\mathrm{c}} = f_{\mathrm{bc}}/f_{\mathrm{c}} = 1.5 \cdot f_{\mathrm{c}}^{-0.075} \tag{44}$$

Since the plastic potential function coefficients are calibrated on the basis of a single triaxial stress state of arbitrary confinement level (here: $\sigma_{\mathrm{pc}} = f_{\mathrm{c}}$), it should be investigated whether the strain amplifications ($\varepsilon_{\mathrm{cc}}/\varepsilon_{\mathrm{c}}$), calculated by the constitutive model, are linearly related to the confinement level ($\sigma_{\mathrm{pc}}/f_{\mathrm{c}}$), as already suggested by Eq. (41). A parametric study has shown that selecting a cubic plastic potential function ($n = 3$) fulfils the above expectation (Fig. 16) and hence an arbitrary selection of the confinement level for the calibration of plastic potential coefficients does not affect the analysis results.

Fig. 17 shows the plastic strain vector directions for uniaxial, triaxial and equibiaxial compression, resulting from the above calibration procedure. It is observed that with increasing confinement, the direction of the plastic strain vector approaches that of the deviatoric axis and hence the rate of volumetric growth (dilatancy) is decreasing. This in turn results in a slower accumulation of plastic volumetric strain (i.e. the hardening/softening parameter κ) and hence increased deformation capacity in both the axial and lateral directions, under triaxial compression. Fig. 18 shows the evolution of the plastic potential surface during hardening and softening (for zero attraction $a = 0$) and Fig. 19 depicts the non-associative characteristics of the plastic flow under uniaxial compression (hardening regime), where it is clear that using an associated flow rule ($f = g$) would result in an overestimation of the plastic dilatancy of concrete (e.g. Kang and Willam, 1999). It has to be noted here that the slight concativity of the plastic potential surface near zero deviatoric length (ρ), which depends on the plastic-potential order and the value of the hardening/softening parameter, is not found

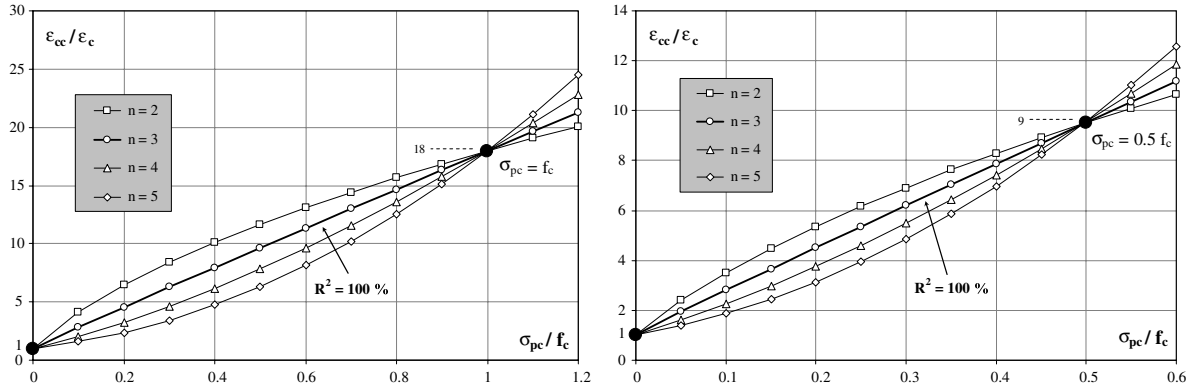

Fig. 16. Selection of the plastic potential function order (for arbitrary confinement levels of 100% and 50%).

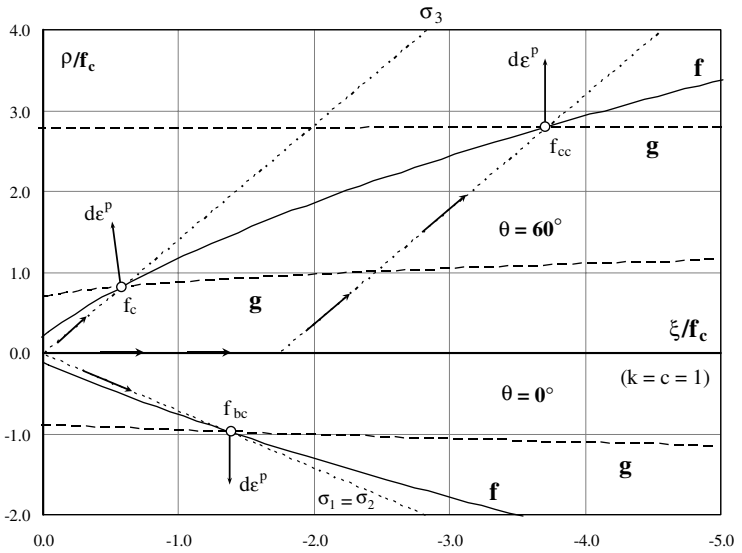

Fig. 17. Direction of the plastic stain vector under uniaxial, triaxial and equibiaxial compression.

to introduce any numerical instabilities under compressive load paths (Figs. 17 and 19), on which the present model is currently focused.

6. Numerical integration

For the integration of the constitutive equations, an implicit backward-Euler return-mapping algorithm was applied (e.g. Macari et al., 1997), incorporating a regula-falsi/secant iterative scheme (Červenka et al., 1998). In order to maintain consistency with constitutive equations, the above scheme iteratively updates the following variables: (1) the plastic multiplier ($d\lambda$) which yields both the stress corrector ($-d\lambda \mathbf{D} m_{ij}^k$) and the additional plastic strains ($+d\lambda m_{ij}^k$), (2) the return direction (m_{ij}^k) of the stress vector towards the failure surface and (3) the hardening/softening functions ($k(\kappa), c(\kappa)$), which control the position and the size of the failure surface (f) and the plastic potential surface (g) in the stress space. The input data (step: n) are the current stress tensor (${}^n\sigma_{ij}$), the plastic strain tensor (${}^n\varepsilon_{ij}^p$), describing the deformation history (load path dependency) of the material, and the trial total strain increment ($d\varepsilon_{ij}$). The output data (step: $n+1$) are the updated nonlinear stress tensor (${}^{n+1}\sigma_{ij}$) and the updated plastic strain tensor (${}^{n+1}\varepsilon_{ij}^p$). The suggested algorithm

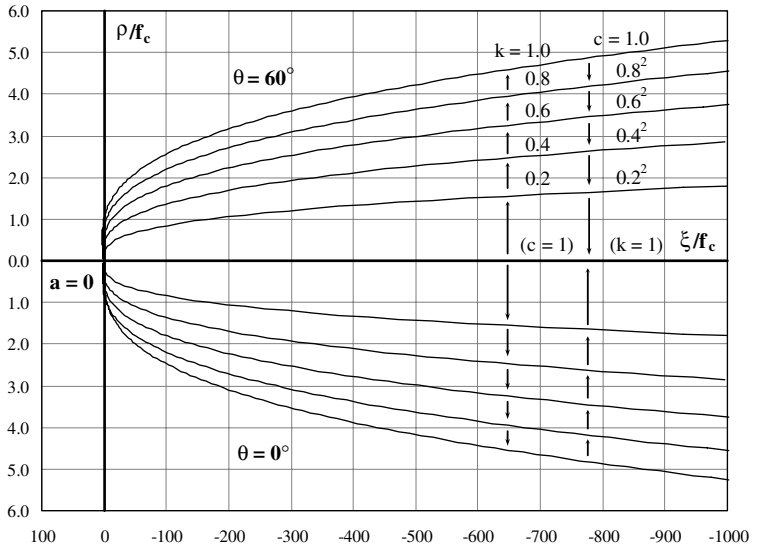

Fig. 18. Evolution of the plastic potential surface during hardening and softening on the Rendulic plane.

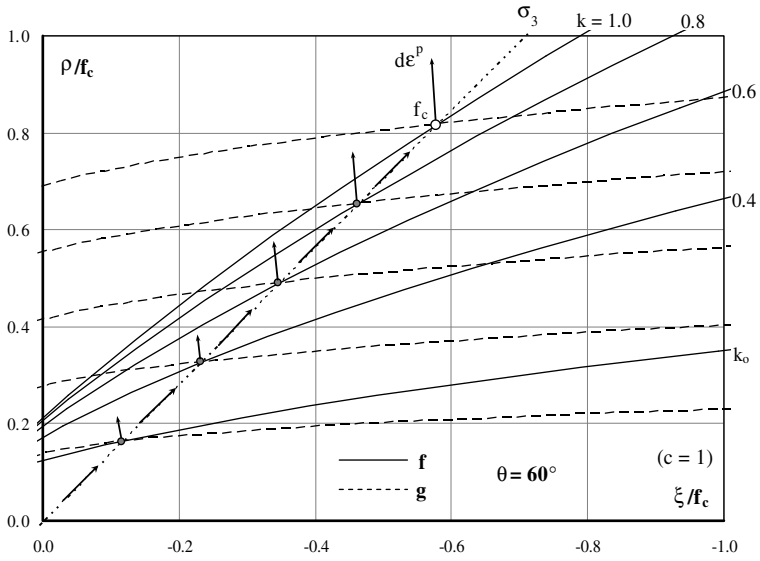

Fig. 19. Non-associated plastic flow under uniaxial compression (hardening regime) on the Rendulic plane.

is numerically stable with a fast rate of convergence, it is independent of the load step size and does not require the differentiation of the failure surface. A detailed flow chart of the procedure is shown in Fig. 20.

In the context of the finite element method, either the initial (elastic) or the tangent stiffness (full Newton–Raphson) approach can be applied in the global solution. For the second case, the tangent stiffness matrix ($\mathbf{D}^{ep}$) of the constitutive model can be derived as follows:

$$\mathbf{D}^{ep} = \mathbf{D} - \frac{\mathbf{D}\cdot\frac{\partial g}{\partial \boldsymbol{\sigma}}\cdot\frac{\partial f}{\partial \boldsymbol{\sigma}}^{T}\cdot\mathbf{D}}{\frac{\partial f}{\partial \boldsymbol{\sigma}}^{T}\cdot\mathbf{D}\cdot\frac{\partial g}{\partial \boldsymbol{\sigma}} - \frac{\partial f}{\partial \kappa}\cdot\boldsymbol{\delta}^{T}\cdot\frac{\partial f}{\partial \boldsymbol{\sigma}}} \tag{45}$$

The calculation of the tangent stiffness matrix definitely increases the computational cost for each Gauss point because it requires the differentiation of the failure surface with respect to the stresses and the hardening/softening parameter. Nevertheless, this would be compensated by the reduced computational cost per iteration in the global solution.

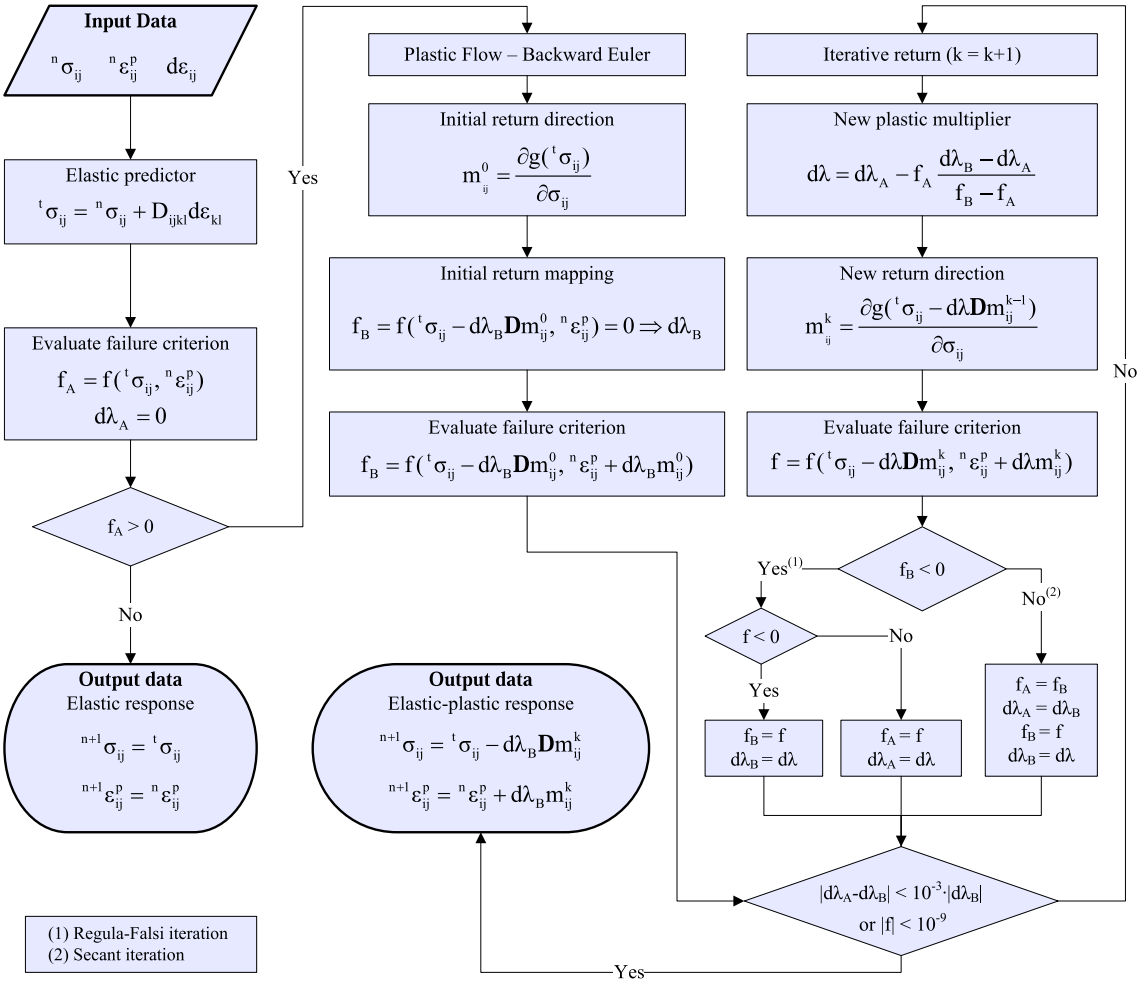

Fig. 20. Flow chart of the backward-Euler return-mapping algorithm.

7. Verification

The present concrete constitutive model was implemented in a stand-alone software application, including a constitutive driver operating at the material stress–strain level. Its performance is evaluated for both normal and high-strength concrete, by comparisons with uniaxial, biaxial and triaxial compressive experimental tests from the literature. It has to be noted here that all model parameters were calibrated only on the basis of the compressive concrete strength (f_c) reported in the respective experimental studies, following the procedures described in the previous sections (generic calibration). Consequently, any discrepancies between analytical and experimental results are mainly attributed to the intrinsic scatter of the experimental results used for calibrating the model parameters (e.g. Figs. 3, 5, 11, 14 and 15). Notwithstanding this scatter, the model structure allows easy recalibration against specific experimental datasets, which can enhance the model performance (targeted calibration). Nonetheless, the suggested generic calibration procedure is deemed adequate for practical purposes, since usually no detailed experimental data is available.

Prior to comparing with experimental results, the numerical performance of the constitutive driver was evaluated against stress–strain pairs of maximum compressive strength and corresponding axial total strain that were directly calculated from the various calibration equations (e.g. (38), (41) and (44)). Fig. 21 shows a set of normalized axial stress–strain curves for concrete under uniaxial, equibiaxial and triaxial compression

for various confinement levels. It is observed that these curves pass from the anticipated stress–strain pairs and therefore, the reliability of the constitutive driver is validated.

Fig. 22 shows a comparison between analytical results (using generic calibration) and experimental results (Dahl, 1992) for normal and high-strength concrete under uniaxial compression. For normal concrete, correlation is reasonable, while for high-strength concrete it is observed that experimental results show lower deformation capacity. However, if the model calibration is targeted, i.e. the values of E_c, ε_c and t are calibrated to correspond to each experimental curve (instead for Eqs. (15), (38) and (20), respectively), the above discrepancies are significantly reduced (Fig. 23).

Fig. 24 shows a comparison between analytical (generic calibration) and experimental results (Kupfer et al., 1969) for concrete under uniaxial compression, in both the axial and lateral directions. The correlation is reasonable, and the relatively small difference regarding the lateral direction is due to the model assumption of zero volumetric strain at maximum stress (Eq. 16), which is not reflected in this experimental study. Moreover, the initial plastic compaction (negative plastic volumetric strain) that is apparent in the volumetric curve

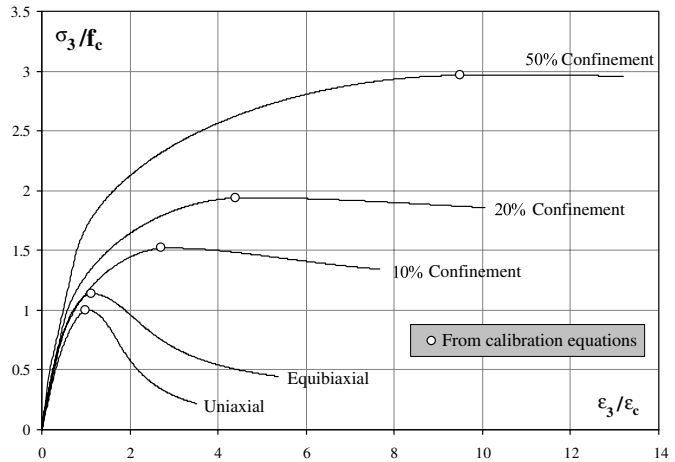

Fig. 21. Comparison between constitutive driver analysis and stress–strain pairs directly calculated from calibration equations.

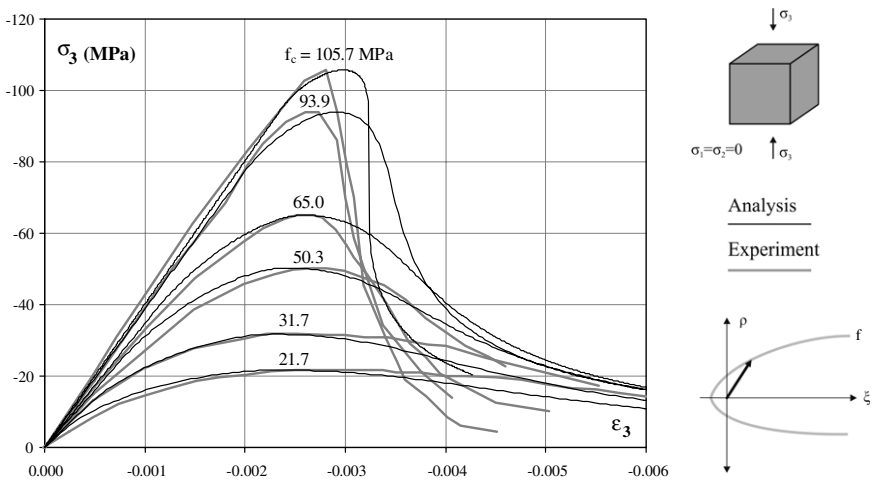

Fig. 22. Comparison between analytical (with generic model calibration) and experimental results (Dahl, 1992) for normal and high-strength concrete under uniaxial compression.

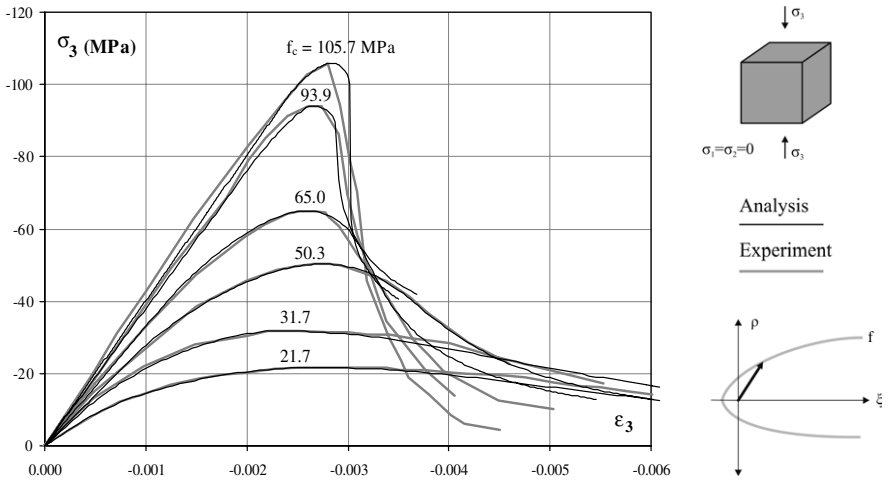

Fig. 23. Comparison between analytical (with targeted model calibration) and experimental results (Dahl, 1992) for normal and high-strength concrete under uniaxial compression.

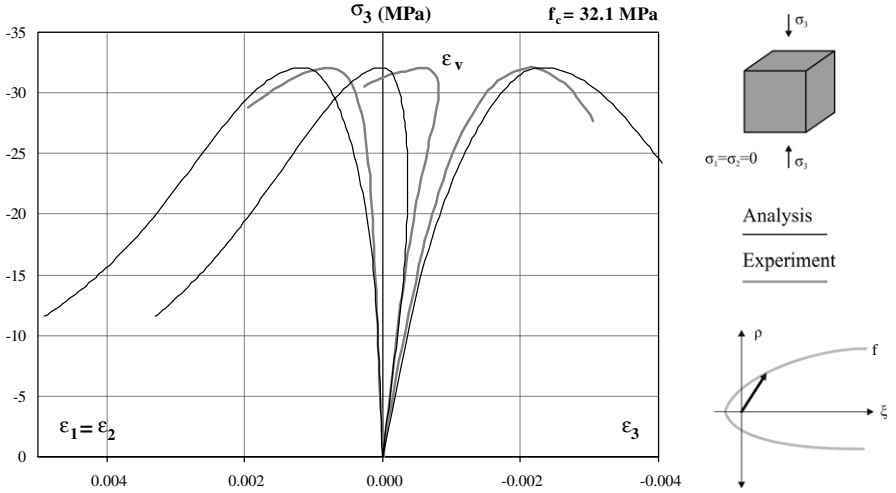

Fig. 24. Comparison between analytical and experimental results (Kupfer et al., 1969) for concrete under uniaxial compression in both axial and lateral directions.

(σ_3–ε_v) cannot be accounted for by the present model structure (plastic volumetric strains are always positive; Fig. 9).

Figs. 25 and 26 show comparisons between analytical and experimental results for normal and high-strength concrete, respectively, under equibiaxial compression (generic calibration). The axial stress–strain behaviour is captured well, while the lateral strain is moderately overestimated. It has to be noted here that in the case of high-strength concrete, the respective experimental test (Hussein and Marzouk, 2000) showed minimal strain amplification under equibiaxial compression, which points to the necessity of the Lode-angle dependent plastic potential function, incorporated in the model. Moreover, any softening behaviour was not captured in this test, hence any comparison beyond maximum strength was meaningless.

Figs. 27 and 28 show comparisons between analytical and experimental results for normal and high-strength concrete, respectively, under triaxial compression and various confinement levels. The observed

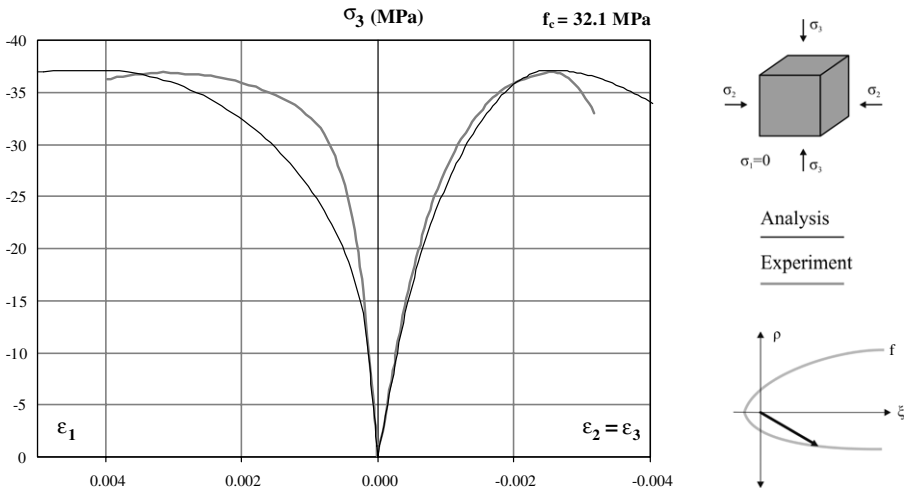

Fig. 25. Comparison between analytical and experimental results (Kupfer et al., 1969) for normal concrete under equibiaxial compression.

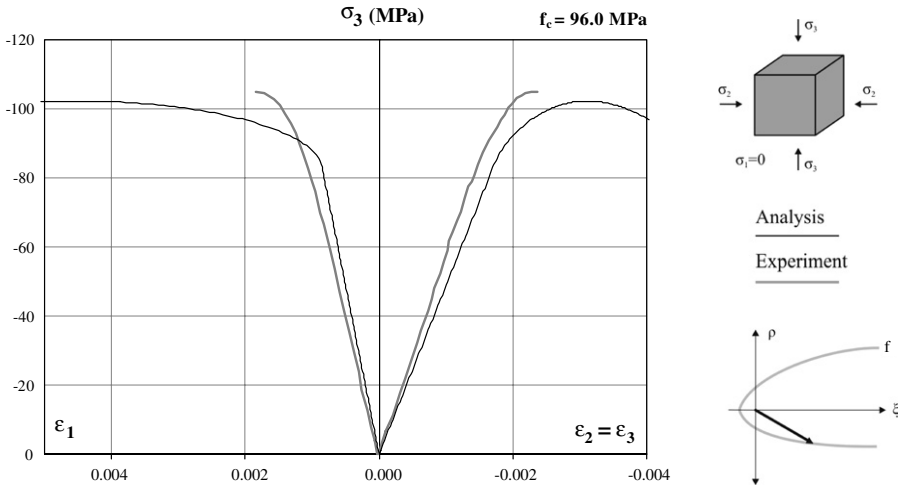

Fig. 26. Comparison between analytical and experimental results (Hussein and Marzouk, 2000) for high-strength concrete under equibiaxial compression.

correlation is acceptable for both the axial and lateral directions, since the respective experimental data are relatively close to the suggested generic calibration equations.

The opposite trend is shown in Fig. 29, where the generic calibration cannot approximate well the strength and deformational characteristics of the high-strength concrete used in the respective experimental study (Xie et al., 1995). Nevertheless, a targeted calibration using some modified model parameters (Table 3) that match the experimentally measured values and hence are not affected by the intrinsic scatter in the generic calibration equations, seems to subdue the above discrepancies (Fig. 30); the remaining model parameters that are not referred in Table 3 follow the generic calibration scheme, as described in the previous sections. Note that E_c and ε_c are material characteristics from standard compression tests, while ε_{cc} is taken from one triaxial test (here for $\sigma_1 = \sigma_2 = 29.3$ MPa), and f_t is not the experimentally derived value, but rather the optimal value calibrated against the experimentally measured triaxial strengths (here $f_c/f_t = 12.5$, see also Section 3). Even better match would have resulted if additional model parameters (such as σ_{co} and t) were also modified (using a trial-and-error approach).

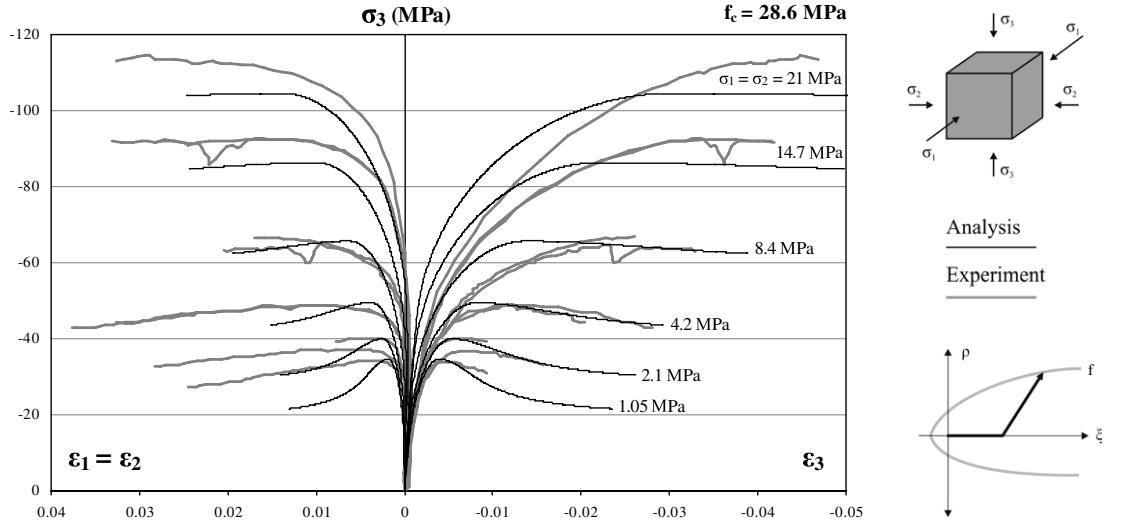

Fig. 27. Comparison between analytical and experimental results (Imran, 1994) for normal concrete under triaxial compression and various confinement levels.

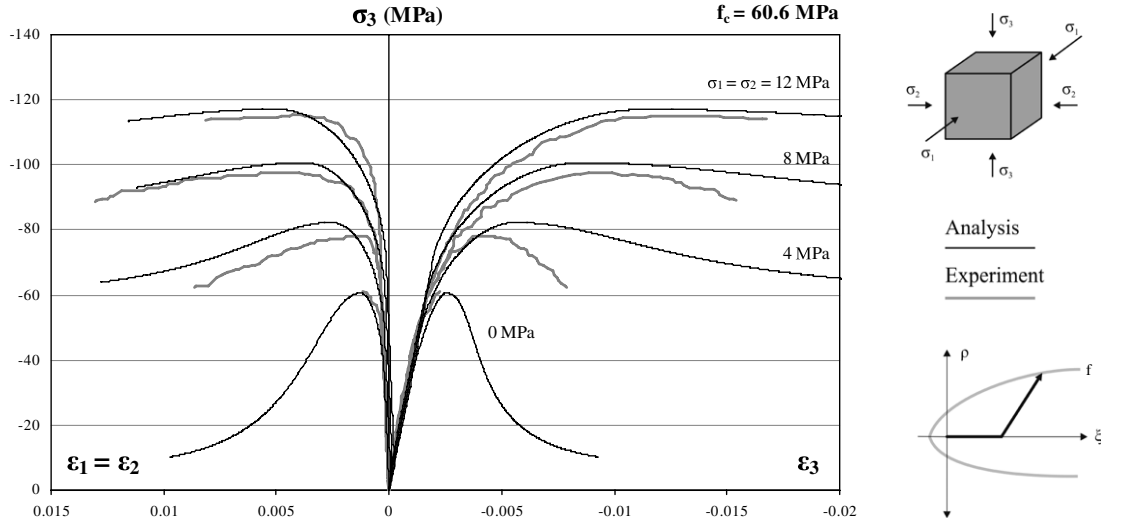

Fig. 28. Comparison between analytical and experimental results (Candappa et al., 2000) for high-strength concrete under triaxial compression and various confinement levels.

8. Conclusions

A confinement-sensitive plasticity constitutive model for concrete in triaxial compression was presented in this study, composed by a three-parameter loading surface, uncoupled hardening and softening functions following the accumulation of plastic volumetric strain, and a nonlinear plastic potential function. The main advantages of the proposed model compared to previous studies are the Lode-angle dependency of the plastic potential function, which allows the calibration of the strain amplifications under equibiaxial compression (tensile meridian), the variable order of the plastic potential function, which controls the experimentally verified linearity between lateral stress and strength amplifications under triaxial compression and the refined softening function, which better reflects the experimentally observed softening behaviour of concrete.

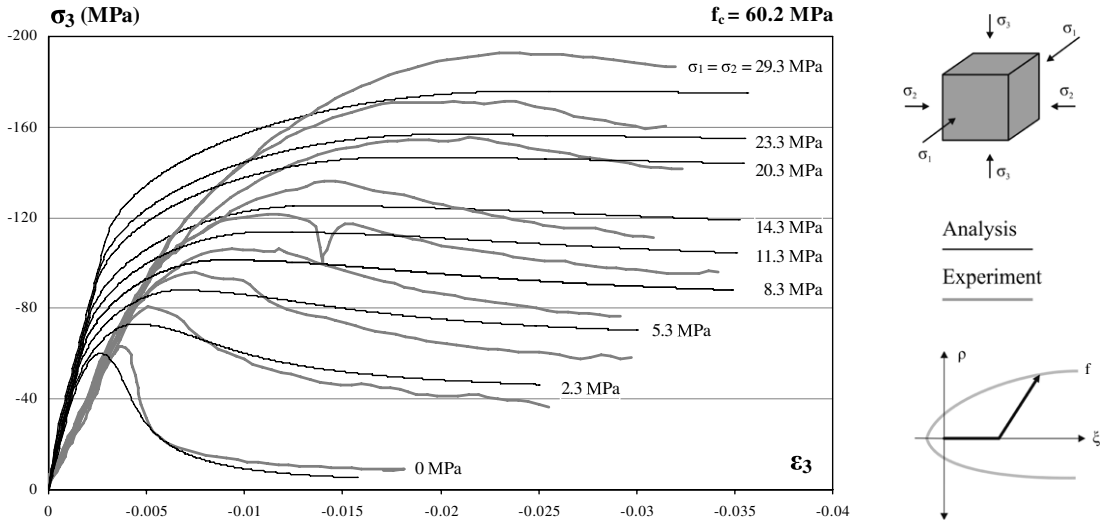

Fig. 29. Comparison between analytical and experimental results (Xie et al., 1995) for high-strength concrete under triaxial compression and various confinement levels (generic calibration).

Table 3
Modification of some model parameters, targeted on the experimental results of Xie et al. (1995)

Parameter	Generic	Targeted
f_c	60.2	60.2
E_c	33927	17500
f_t	6.02	4.82
ε_c	−0.0025	−0.0035
ε_{cc}	−0.0370	−0.0235

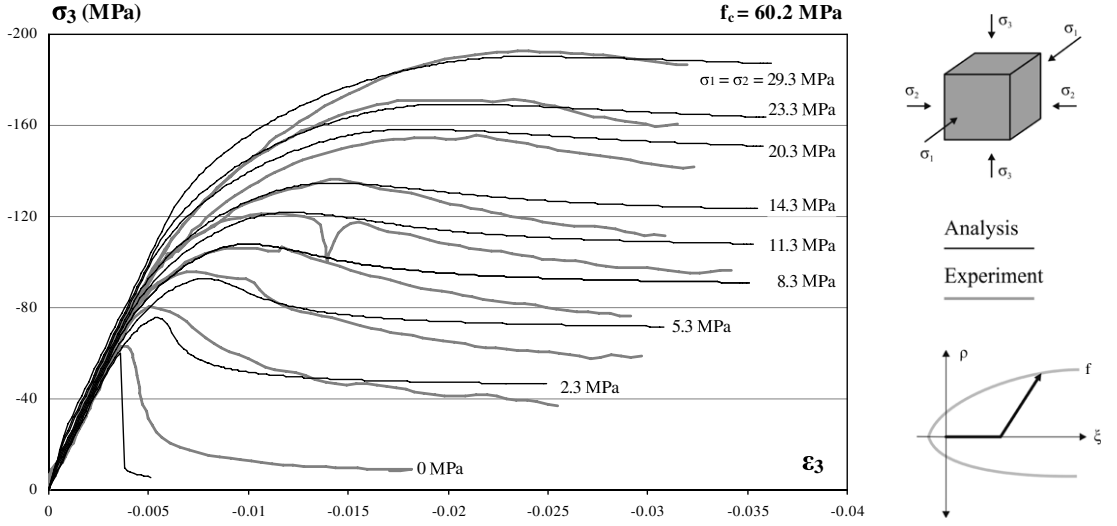

Fig. 30. Comparison between analytical and experimental results (Xie et al., 1995) for high-strength concrete under triaxial compression and various confinement levels (targeted calibration).

Key model parameters were calibrated against an ad hoc compiled database of test results, which is substantially expanded with respect to similar databases used by previous investigators. Furthermore, this generic calibration scheme was also based on code recommendations, eventually rendering the various model parameters dependent only on the uniaxial compressive concrete strength. The model performance was evaluated against experimental results and it was verified that the ultimate strength, deformation capacity and residual strength of confined concrete were properly captured.

An important further aspect of the suggested model is that it follows an open structure, allowing easy recalibration using selected experimental datasets, in order to enhance its performance in specific cases. Furthermore, it may be combined with a fracture tensile model in order to globally simulate the concrete behavioural characteristics under multiaxial stress states. This aspect is currently being pursued by the writers.

Figs. 3–6, 11, 14 and 15 contain experimental results from the following sources: Ansari and Li (1998), Attard and Setunge (1996), Balmer (1949), Chinn and Zimmerman (1965), Endebrock and Traiana (1972), Harries and Kharel (2003), Hognestad et al. (1955), Kotsovos and Newman (1980), Lan and Guo (1999), Mills and Zimmerman (1970), Nawy et al. (2003), Nelissen (1972), Ramaley and McHenry (1947), Richart et al. (1928), Schickert and Winkler (1977), Smith and Young (1956), Su and Hsu (1998), Tasuji et al. (1978), Traina (1983), Wang et al. (1978), Wee et al. (1996).

Acknowledgements

This work has been performed within the framework of the research project 'ASProGe: Seismic Protection of Bridges', funded by the General Secretariat of Research and Technology (GGET) of Greece.

Appendix A. Notation

a	attraction parameter of the plastic potential function
A	first coefficient of the plastic potential function
B	second coefficient of the plastic potential function
C	third coefficient of the plastic potential function
$c(\kappa)$	softening function
$\mathbf{D}$, D_{ijkl}	elasticity matrix
$\mathbf{D}^{ep}$	elastoplastic tangent stiffness matrix
d	incremental representation of vectors and tensors
$d\lambda$	plastic multiplier
e	eccentricity parameter of out-of-roundness
e^{p}	plastic deviatoric strain
E_c	concrete elastic modulus
f	loading function
f_{bc}	equibiaxial compressive concrete strength
f_c	mean uniaxial compressive concrete strength
f_{cc}	triaxial compressive concrete strength
f_t	mean uniaxial tensile concrete strength
g	plastic potential function
I_1	first invariant of the stress tensor
J_2	second invariant of the deviatoric stress tensor
J_3	third invariant of the deviatoric stress tensor
$k(\kappa)$	hardening function
k_o	hardening parameter defining the onset of plastic flow
m	friction parameter of the loading function
n	order of the plastic potential function
n_1	first parameter of softening function (Eq. (18))
n_2	second parameter of softening function (Eq. (19))
$r(\theta, e)$	elliptic function of the loading function

t	slope parameter of the softening function
$\boldsymbol{\delta}$	Kronecker delta
$\boldsymbol{\varepsilon}$, ε_{ij}	total strain vector and tensor
ε_c	total strain at uniaxial concrete strength
ε_{bc}	total strain at equibiaxial concrete strength
ε_{cc}	total strain at triaxial concrete strength
$\boldsymbol{\varepsilon}^e$, ε^e_{ij}	elastic strain vector and tensor
$\boldsymbol{\varepsilon}^p$, ε^p_{ij}	plastic strain vector and tensor
ε_v	total volumetric strain
ε^p_v	plastic volumetric strain
$\varepsilon^p_{v,t}$	plastic volumetric strain at uniaxial concrete strength (threshold value)
θ	Lode angle of the stress vector in Haigh–Westergaard stress space
κ	hardening/softening parameter
v	concrete Poisson's ratio
ξ	hydrostatic length of the stress vector in Haigh–Westergaard stress space
ξ'	hydrostatic length of the plastic strain vector
ρ	deviatoric length of the stress vector in Haigh–Westergaard stress space
ρ'	deviatoric length of the plastic strain vector
$\boldsymbol{\sigma}$, σ_{ij}	stress vector and tensor
σ_{co}	concrete stress defining the onset of plastic flow
σ_{pc}	lateral (confinement) concrete stress
ψ	inclination of the plastic strain vector

Appendix B. Partial derivatives of the plastic potential function (g)

For the definition of the plastic flow rule (Eq. (3)), the partial derivatives of the plastic potential function with respect to the principal stresses are:

$$\frac{\partial g}{\partial \sigma_1} = \frac{n \cdot A}{(k \cdot \sqrt{c} \cdot f_c)^n} \cdot (2J_2)^{\frac{n}{2}-1} \cdot \frac{2 \cdot \sigma_1 - \sigma_2 - \sigma_3}{3} + \frac{\left[C + \frac{1}{2}(B-C)(1-\cos 3\theta)\right]}{k \cdot \sqrt{c} \cdot f_c} \cdot \frac{1}{\sqrt{2J_2}} \cdot \frac{2 \cdot \sigma_1 - \sigma_2 - \sigma_3}{3} + \frac{1}{\sqrt{3} \cdot k \cdot \sqrt{c} \cdot f_c}$$

$\frac{\partial g}{\partial \sigma_2}$, $\frac{\partial g}{\partial \sigma_3}$ same as above using cyclic references for σ_2 and σ_3.

References

Ansari, F., Li, Q., 1998. High-strength concrete subjected to triaxial compression. ACI Materials Journal 95 (6), 747–755.

Attard, M.M., Setunge, S., 1996. Stress strain relationship of confined and unconfined concrete. ACI Materials Journal 93 (5), 1–11.

Balmer, G.G., 1949. Shearing strength of concrete under high triaxial stress—computation of Mohr's envelope as a curve. Structural Research Laboratory Report, No SP-23, United States Department of the Interior, Bureau of Reclamation, Washington, DC.

Barros, M., 2001. Elasto-plastic modelling of confined concrete elements following MC90 equations. Engineering Structures 23 (4), 311–318.

Bažant, Z.P., Prat, P.C., 1988. Microplane model for brittle–plastic material: I. Theory. Journal of Engineering Mechanics, ASCE 114 (10), 1672–1688.

Candappa, D.C., Sanjayan, J.G., Setunge, S., 2000. Complete triaxial stress–strain curves of high-strength concrete. Journal of Materials in Civil Engineering, ASCE 13 (3), 209–215.

Carreira, D.J., Chu, K.H., 1985. Stress–strain relationship for plain concrete in compression. ACI Journal 82 (6), 797–804.

CEB, 1993. CEB/FIP Model Code 1990. Bulletin d' Information CEB, 213/214, Lausanne.

CEB Working Group on HSC/HPC, 1995. High performance concrete—recommended extensions to the model code 90—research needs, Bulletin d' Information CEB, 228, Lausanne.

Červenka, J., Červenka, V., Eligehausen, R., 1998. Fracture-plastic material model for concrete. Application to analysis of powder actuated anchors. In: Mihashi, H., Rokugo, K. (Eds.), . In: Proceedings of the 3rd International Conference on Fracture Mechanics of Concrete Structures—FraMCoS 3, Gifu, Japan, vol. 2. Aedificatio Publishers, Freiburg, Germany, pp. 1107–1116.

Chen, W.F., Han, D.J., 1988. Plasticity for Structural Engineers. Springer-Verlag, New York.
Chinn, J., Zimmerman, R.M., 1965. Behavior of plain concrete under various high triaxial compression loading conditions, Technical Report WL TR 64-163, Air Force Weapons Laboratory, New Mexico.
Dahl, K.K.B., 1992. A constitutive model for normal and high-strength concrete. ABK Report No. R287, Department of Structural Engineering, Technical University of Denmark.
Darwin, D., Pecknold, D.A., 1977. Nonlinear biaxial stress–strain law for concrete. Journal of Engineering Mechanics, ASCE 103 (2), 229–241.
De Borst, R., 1986. Non-linear analysis of frictional materials, Ph.D. Thesis, Delft University of Technology.
Endebrock, E.G., Traiana, L.A., 1972. Static concrete constitutive relations based on cubical specimens, Air Force Weapon Lab, Technical Report No. AFWL-TR-72-59, vol. I and II, Kirtland Air Force Base, New Mexico.
Grassl, P., Lundgren, K., Gylltoft, K., 2002. Concrete in compression: a plasticity theory with a novel hardening law. International Journal of Solids and Structures 39 (20), 5205–5223.
Grassl, P., Jirasek, M., 2006. Damage-plastic model for concrete failure. International Journal of Solids and Structures 43 (22–23), 7166–7196.
Han, D.J., Chen, W.F., 1985. A nonuniform hardening plasticity model for concrete materials. Mechanics of Materials 4 (3–4), 283–302.
Harries, K.A., Kharel, G., 2003. Experimental investigation of the behavior of variably confined concrete. Cement and Concrete Research 33 (6), 873–880.
Hognestad, E., Hanson, N.W., McHenry, D., 1955. Concrete stress distribution in ultimate strength design. ACI Journal 52 (4), 455–480.
Hussein, A., Marzouk, H., 2000. Behavior of high-strength concrete under biaxial stress. ACI Materials Journal 97 (1), 27–36.
Imran, I., 1994. Applications of nonassociated plasticity in modeling the mechanical response of concrete, PhD Thesis, Department of Civil Engineering, University of Toronto.
Imran, I., Pantazopoulou, S.J., 1996. Experimental study of plain concrete under triaxial stress. ACI Materials Journal 93 (6), 589–601.
Imran, I., Pantazopoulou, S.J., 2001. Plasticity model for concrete under triaxial compression. Journal of Engineering Mechanics, ASCE 127 (3), 281–290.
Kang, H.D., Willam, K.J., 1999. Localization characteristics of triaxial concrete model. Journal of Engineering Mechanics, ASCE 125 (8), 941–950.
Kotsovos, M.D., Newman, J.B., 1980. A mathematical description of deformational behavior of concrete under generalized stress beyond ultimate strength. ACI Journal 77 (5), 340–346.
Kupfer, H., Hilsdorf, K., Rusch, H., 1969. Behavior of concrete under biaxial stresses. ACI Journal 66 (8), 656–666.
Lan, S., Guo, Z., 1999. Biaxial compression behavior of concrete under repeated loading. Journal of Materials in Civil Engineering, ASCE 11 (2), 105–115.
Lee, S.K., Song, Y.C., Han, S.H., 2004. Biaxial behavior of plain concrete of nuclear containment building. Nuclear Engineering and Design 227 (2), 143–153.
Liu, T.C.Y., Nilson, A.H., Slate, F.O., 1972. Stress–strain response and fracture of concrete in uniaxial and biaxial compression. ACI Journal 69 (5), 291–295.
Macari, E.J., Weihe, S., Arduino, P., 1997. Implicit integration of elastoplastic models for frictional materials with highly non-linear hardening functions. Mechanics of Cohesive-Frictional Materials 2 (1), 1–29.
Menétrey, P., Willam, K.J., 1995. Triaxial failure criterion for concrete and its generalization. ACI Structural Journal 92 (3), 311–318.
Mills, L.L., Zimmerman, R.M., 1970. Compressive strength of plain concrete under multiaxial loading conditions. ACI Journal 67 (10), 802–807.
Nawy, E.G., Lim, D.H., McPherson, K.L., 2003. Compressive behavior of high-strength high-performance concrete under biaxial loading. ACI Special Publication 213, 43–60.
Nelissen, L.J.M., 1972. Biaxial testing of normal concrete. Heron (Delft) 18 (1), 90.
Ohtani, Y., Chen, W.F., 1989. A plastic-softening model for concrete materials. Computers and Structures 33 (4), 1047–1055.
Ottosen, N.S., 1977. A failure criterion for concrete. Journal of Engineering Mechanics Division, ASCE 103 (4), 527–535.
Papanikolaou, V.K, Kappos, A.J., 2005. Modelling confinement in concrete columns and bridge piers through 3D nonlinear finite element analysis. In: *fib* Symposium Keep Concrete Attractive, Budapest, Hungary, May 2005, pp. 488–495.
Ramaley, D., McHenry, D., 1947. Stress–strain curves for concrete strained beyond ultimate load. Laboratory Report No. SP-12, U.S. Bureau of Reclamation, Denver, 23pp.
Rashid, M.A., Mansur, M.A., Paramasivam, P., 2002. Correlations between mechanical properties of high-strength concrete. Journal of Materials in Civil Engineering, ASCE 14 (3), 230–238.
Richart, F.E., Brandtzaeg, A., Brown, R.L., 1928. A study of the failure of concrete under combined compressive stresses. Engineering Experiment Station Bulletin, No. 185, University of Illinois, Urbana.
Schickert, G., Winkler, H., 1977. Results of test concerning strength and strain of concrete subjected to multiaxial compressive stresses. Deutscher Ausschuss fur Stahlbeton, Heft 277, Berlin, West Germany.
Sfer, D., Carol, I., Gettu, R., Etse, G., 2002. Study of the behavior of concrete under triaxial compression. Journal of Engineering Mechanics, ASCE 128 (2), 156–163.
Smith, G.M., Young, L.E., 1956. Ultimate flexural analysis based on stress–strain curves of cylinders. ACI Journal 53 (6), 597–609.
Smith, S.S., Willam, K.J., Gerstle, K.H., Sture, S., 1989. Concrete over the top, or is there life after peak? ACI Materials Journal 86 (5), 491–497.
Su, E.C.M., Hsu, T.T.C., 1998. Biaxial compression fatigue and discontinuity of concrete. ACI Materials Journal 85 (3), 178–188.

Tasuji, M.E., Slate, F.O., Nilson, A.H., 1978. Stress–strain response and fracture of concrete in biaxial loading. ACI Journal 75 (7), 306–312.

Traina, L.A., 1983. Experimental stress–strain behavior of a low strength concrete under multiaxial states of stress, Air Force Weapon Lab, Technical Report No. AFWL-TR-72-59, vol. I and II, Kirtland Air Force Base, New Mexico.

Traina, L.A., Mansour, S.A., 1991. Biaxial strength and deformational behavior of plain and steel fiber concrete. ACI Materials Journal 88 (4), 354–362.

Van Gysel, A., Taerwe, L., 1996. Analytical formulation of the complete stress–strain curve for high strength concrete. Materials and Structures, RILEM 29 (193), 529–533.

Van Mier, J.G.M., 1986. Multiaxial strain softening of concrete. Part I: fracture. Materials and Structures RILEM 19 (111), 179–190.

Wang, P.T., Shah, S.P., Naaman, A.E., 1978. Stress–strain curves of normal and lightweight concrete in compression. ACI Journal 75 (11), 603–611.

Wee, T.H., Chin, M.S., Mansur, M.A., 1996. Stress–strain relationship of high-strength concrete in compression. Journal of Materials in Civil Engineering, ASCE 8 (2), 70–76.

Xie, J., Elwi, A.E., MacGregor, J.G., 1995. Mechanical properties of three high-strength concretes containing silica fume. ACI Materials Journal 92 (2), 135–145.

Yin, W.S., Su, E.C.M., Mansur, M.A., Hsu, T.T.C., 1989. Biaxial tests of plain and fiber concrete. ACI Materials Journal 86 (3), 236–243.